Effective toughness of periodic heterogeneous materials: the effect of out-of-plane excursions of cracks

Mathias Lebihain, Jean-Baptiste Leblond, Laurent Ponson

Effective toughness of periodic heterogeneous materials: the effect of out-of-plane excursions of cracks

Mathias Lebihain[a,b], Jean-Baptiste Leblond[a], Laurent Ponson[a]

[a]*Institut Jean le Rond ∂'Alembert (Sorbonne Université, UPMC, CNRS UMR 7190), 4 Place Jussieu, 75005 Paris, France*
[b]*Laboratoire Navier (Université Paris-Est, ENPC, IFSTTAR, CNRS UMR 8205), 6-8 avenue Blaise Pascal, 77455 Marne-la-Vallée, France*

Abstract

A powerful semi-analytical method is developed to investigate the impact of tough inclusions on crack paths and the resulting effective fracture properties. Using a perturbative approach of fracture mechanics, this method allows to account for out-of-plane excursions of cracks resulting from the discontinuity of toughness at the inclusion/matrix interface, by applying a generalized maximum-energy-release-rate criterion. For a sufficiently large toughness mismatch between the matrix and the inclusions, the crack by-passes the obstacles, thus reducing the inclusion-induced reinforcement of the material. For spherical inclusions, obstacles of fracture energy larger than 3.85 times that of the matrix become ineffective to further reinforce the material, because of their systematic by-pass. The role played by the shape of the inclusions is also investigated; inclusions of non-spherical shape may reduce the reinforcement through three-dimensional collective effects emerging from the coupling between the in-plane and out-of-plane components of the crack front perturbation. Finally we show that inclusion by-pass not only limits crack bowing but can also prevent crack bridging, for inclusions short enough in the direction orthogonal to the mean fracture plane. Thus this study provides a quantitative picture of the interaction mechanisms between a crack front and tough inclusions, which paves the way to the future microstructural design of brittle solids with improved resistance to failure.

Keywords: Brittle fracture, heterogeneous materials, effective toughness, homogenization methods, toughening mechanisms

1. Introduction

The development of a microstructure-sensitive theory of fracture has been a challenge for decades in solids mechanics. Today, the boom of additive manufacturing techniques and the emergence of bio-source and recycled composite materials driven by environmental concerns have increased further the need to rationalize the failure behavior of micro-structured solids (Reis, 2006; Jo et al., 2008; Dimas et al., 2013; Wang and Xia, 2017). Yet, a comprehensive theoretical framework that allows for the *ab initio* prediction of the toughness of materials from their microstructural features is still lacking.

*Corresponding author : mathias.lebihain@enpc.fr

Recently renewed attention has been paid to the fracture behavior of heterogeneous materials, see e.g. Barthelat and Rabiei (2011), Patinet et al. (2013), Démery et al. (2014) , Hossain et al. (2014), Xia et al. (2015), Vasoya et al. (2016a) and Wang and Xia (2017). These studies aim at describing quantitatively the impact of small scale microstructural features of materials on their macroscopic failure properties, thus paving the way for a comprehensive fracture mechanics theory of heterogeneous media. They can be viewed as the continuation of pioneer works dedicated to the interaction mechanisms between a macroscopic crack and a tough inclusion, notably crack trapping (Gao and Rice, 1989; Bower and Ortiz, 1990), crack deflection (Faber and Evans, 1983; Suresh, 1985; Rödel, 1992) and crack bridging (Erdogan and Joseph, 1989; Bower and Ortiz, 1991), that occur during the failure of particle-reinforced ceramics. But they also embrace a broader ambition related to the development of a general micromechanical theory of fracture able to predict the effective toughness of brittle solids from the spatial distribution and mechanical properties of microstructural heterogeneities, in the spirit of the homogenization methods dedicated to elastic and non-linear mechanical properties of materials (Nemat-Nasser et al., 1996; Ponte-Castañeda and Suquet, 1997). This work fully encompasses both perspectives, as

- it aims at providing a quantitative analysis of the reinforcement of brittle solids by tough inclusions, in line with the seminal works on particle-reinforced ceramics quoted above, but also beyond, as it also takes into account the out-of-plane by-pass of particles that largely controls the efficiency of the reinforcement;

- it also provides basic theoretical concepts that will serve as building blocks for the prediction of the effective fracture properties of materials with heterogeneous distributions of toughness, as will be shown notably in a subsequent paper dedicated to the effective toughness of composites with disordered distributions of inclusions (Lebihain et al., 2020).

The in-plane trapping of cracks by tough inclusions was first studied using a perturbative approach based on the Bueckner-Rice weight function theory (Bueckner, 1987; Rice, 1985). Gao and Rice (1989) thus analyzed how periodic arrangements of tough inclusions may reinforce brittle solids by hindering crack propagation. Using the second-order theory of Leblond et al. (2012), Vasoya et al. (2016b) explored the pinning of cracks by tough obstacles beyond the linear approximation. Beyond the first- and second-order approximations, Bower and Ortiz (1991) showed that a sufficiently strong trapping may lead to crack bridging, enhancing further the material resistance to crack growth. Focusing on a penny-shaped crack trapped by an array of radially invariant, very tough obstacles, Vasoya et al. (2016a) evidenced the existence of a fingering instability wherein the front propagates in between the obstacles, letting behind unbroken regions of the interface. Considering randomly distributed fracture properties, Roux et al. (2003), Patinet et al. (2013) and Démery et al. (2014) developed homogenization methods to rationalize the disorder-induced toughening reminiscent of the collective pinning of crack fronts by a large number of impurities. Finally, Xia et al. (2015) and Hsueh and Bhattacharya (2018) used these concepts to functionalize heterogeneous interfaces, through the rational design of obstacles with complex shapes, achieving for example toughness asymmetry. All these works built on efficient analytical or semi-analytical perturbative methods. Yet they were restricted to coplanar crack propagation and thus overlooked the effect of excursions of cracks out of the mean fracture plane, such as inclusion by-pass. Such an effect has been investigated in the works of Ramanathan et al. (1997), Bonamy et al. (2006) and Barès et al. (2014), who introduced an *ad hoc* stochastic shear loading component in the set of perturbative equations governing the crack

evolution, so as to model crack deflections induced by material impurities. Even though these works provided some insight on the roughness properties of the resulting fracture surface, they failed to provide any hint on the effect of the geometry and mechanical properties of the inclusions upon the overall fracture toughness.

Beyond analytical or semi-analytical models, the out-of-plane deflection of cracks by tougher or stiffer inclusions has been studied through the Finite Element (FE) method (Bush, 1997), the Extended Finite Element (XFEM) method (Gao et al., 2017), cohesive zone models (Li and Zhou, 2013; Wang and Xia, 2017; Zeng and Wei, 2017), and phase field models (Hossain et al., 2014; Ylmaz et al., 2018; Bleyer and Alessi, 2018; Li and Maurini, 2019). These various methods allow for a realistic description of microstructural features such as inclusions, and a quantitative description of the resulting reinforcement. Yet, their computational cost is high so they are often limited to a two-dimensional setting (i.e. geometries invariant in the direction of the crack front). As a result, they do not capture in-plane toughening mechanisms like crack bowing or its interaction with out-of-plane growth processes (e.g. inclusion by-pass). Notable exceptions are the works of Clayton and Knap (2014) and Nguyen et al. (2016, 2017b,a) who explored the interaction between a crack and microstructural heterogeneities in a fully three-dimensional setting. However, their calculations were limited to a few inclusions, and furthermore their focus was on crack trajectory, without addressing the impact of this trajectory upon the overall material toughness.

Here, we first develop an efficient theoretical/numerical model, allowing to simulate crack propagation in heterogeneous brittle materials containing arbitrary numbers of inclusions. Leaving applications to situations involving disordered materials with large numbers of inclusions for future studies, we focus here on periodic geometries, with only one inclusion per period, in order to investigate in depth some fundamental aspects of the crack-inclusion interaction problem. Our work reveals the subtle three-dimensional coupling between the in-plane and out-of-plane deformation modes of a crack front during its interaction with a microstructural heterogeneity. We show that it governs the competition between the in-plane crossing of a tough inclusion and its out-of-plane by-pass, that ultimately controls the level of reinforcement. This allows to determine that beyond some critical toughness contrast between the inclusion and the matrix, the particle-induced reinforcement becomes inefficient as the crack by-passes the obstacle. For non-spherical inclusions, we show that the geometry of the inclusion may counter-balance or enhance this effect. More broadly, our study reveals that crack deflection is rarely beneficial to the overall toughness as it can hinder more efficient toughening mechanisms such as crack bowing or crack bridging.

With regard to modeling aspects, more specifically, the three-dimensional coupling between the modes of front distortion is addressed within a Linear Elastic Fracture Mechanics (LEFM) perturbative framework based on the works of Gao and Rice (1986) for the in-plane perturbation of the crack front and (Movchan et al., 1998) for the out-of-plane perturbation of the crack surface. The material microstructure is modeled as distributions of tough inclusions embedded in a weaker matrix. Application of a Generalized Maximum Energy Release Rate (GMERR) criterion (Gurtin and Podio-Guidugli, 1998; Hakim and Karma, 2005; Chambolle et al., 2009) at the toughness discontinuity between the inclusion and the matrix allows to model out-of-place excursions of the crack, without having to introduce an artificial mode II shear loading component as done in the works of Ramanathan et al. (1997), Bonamy et al. (2006) and Barès

et al. (2014). With this fracture mechanisms-based model, the issue of the effective toughness resulting from the interaction between a crack front and inclusions of arbitrary shape and fracture properties (interfacial toughness and inclusion toughness) can be tackled appropriately in a fully three-dimensional setting at a low computational cost.

The paper is organized as follows:

- Section 2 presents the theoretical model combining the definition of the material microstructure, the perturbative three-dimensional LEFM approach permitting the calculation of the stress intensity factors along the front of a crack arbitrarily perturbed both within and out of its plane, the suitable criterion for the prediction of the future local direction of propagation and the kinetic law providing the local velocity of the front.
- Section 3 details the numerical implementation of the model, involving notably an explicit scheme for time-integration, and a convergence criterion for the determination of the suitable time-step.
- Section 4 is dedicated to the analysis of the competition between the crossing and the by-pass of tough spherical inclusions. The transition between one mechanism to another, and its implication on the effective toughness of periodic heterogeneous media is investigated. We show that beyond some critical value of the inclusion toughness, the crack systematically by-passes the obstacle, resulting in a maximum, "plateau" value of the effective toughness no longer depending upon the inclusion toughness.
- In Section 5, subtler weakening mechanisms, resulting from the collective by-pass of inclusions due to the coupling of the in-plane and out-of-plane crack front perturbations, are also evidenced, by considering ellipsoidal prolate inclusions elongated in the direction parallel to the crack front.
- Finally Section 6 discusses the competition between crack bowing, crack deflection and crack bridging, through consideration of the interaction of a crack with prolate obstacles elongated in the direction perpendicular to the fracture plane.

2. Theoretical modeling

In contrast to variational approaches (Francfort and Marigo, 1998; Nguyen et al., 2017b; Bleyer and Alessi, 2018; Li and Maurini, 2019) and phase field models (Hakim and Karma, 2005, 2009), where both questions of crack initiation and propagation are addressed within a "global" approach at the scale of the entire structure, the traditional approach of LEFM, as used in this paper, relies on local propagation criteria using the Stress Intensity Factors ($K_{\mathrm{I}}, K_{\mathrm{II}}, K_{\mathrm{III}}$) (SIFs) and/or the elastic Energy-Release-Rate G (ERR) in combination with the material toughness G_{c}, to predict the crack path and the loading conditions actually inducing propagation. Any predictive method of crack propagation based on this classical framework thus requires three main ingredients, be it in the homogeneous or heterogeneous case, for a mode I loading or mixed-mode conditions :

1. The definition of a given microstructure, which provides, in our specific case, the field $G_{\mathrm{c}}(\mathbf{x})$ of fracture energy experienced by the crack when propagating. Note that with some abuse of terminology, we shall refer to the fracture energy $G_{\mathrm{c}} \equiv \dfrac{1-\nu^2}{E} K_{\mathrm{Ic}}^2$ as the "toughness" of the material.

2. Some way of calculating the SIFs $\left(K_p\right)_{p\in\{\mathrm{I,II,III}\}}$ and the ERR G along the crack front $\mathcal{F}$, for any crack configuration differing slightly from a planar crack with a straight front.
3. Some propagation criteria, combining a prediction of the future direction of propagation and a kinetic law for the crack front advance, based on the previous elements.

The following sections describe how each of these ingredients is accounted for, and how they are connected to each other. In Section 2.1, we describe the microstructures considered and explain how they are generated, including a discussion of the simplifying hypotheses made. Section 2.2 expounds the perturbative three-dimensional LEFM approach used, focusing on the sole case of a semi-infinite crack subjected to some tensile loading. The combination of these two ingredients within a Generalized Maximum Energy Release Rate (GMERR) criterion and a kinetic law is explained in Section 2.3.

2.1. Heterogeneous microstructure and toughness field

We consider an semi-infinite crack embedded in an infinite periodic body. We adopt the usual convention of LEFM and thus denote x the direction of crack propagation, y the direction orthogonal to the crack plane, and z the direction parallel to the crack front $\mathcal{F}$. Also, the period in the z-direction is denoted L_z. The associated unit vectors are denoted $\left(\underline{e}_p\right)$. At a given time t, the position of the crack front within the crack plane is noted $x\,(t)$, the origin O being chosen arbitrarily within this plane (Fig. 1.a).

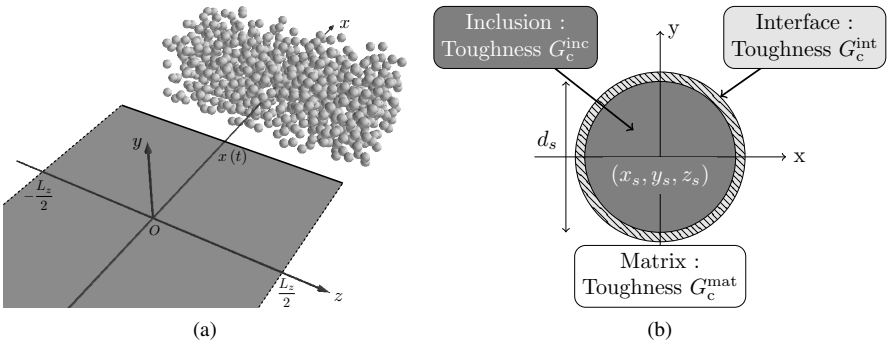

(a) (b)

Figure 1: (a) Semi-infinite crack facing a polydisperse inclusion distribution with varying toughness; (b) Fracture properties of the inclusion, the matrix and their interface.

The material is made of two phases: a homogeneous matrix and spheroidal inclusions. The inclusion distribution $\mathcal{D}$ is defined by the inclusion positions $(x_s, y_s, z_s, d_s)_{s\in[\![1;N]\!]}$. The inclusions are considered to be distributed isotropically and their diameters follow a monodisperse or polydisperse distribution, characterized by its mean value d and standard deviation σ_d.

Two main assumptions are made regarding the mechanical behavior of each phase. First, the matrix and the inclusions are assumed to be isotropically and linearly elastic and share the same Young's modulus E and Poisson's ratio ν. Second, the phases are assumed to be brittle but differ in their fracture properties: the inclusions may be tougher and/or weakly bonded to the matrix. These properties are characterized by an inclusion toughness G_c^{inc} and an interfacial toughness

G_c^{int} as depicted in Fig. 1.b. These fracture properties may vary from one inclusion to another.

A clear separation of lengthscales is assumed between :

- the size of the structure L_{struct} ;
- the inclusion size d (Fig. 1.a);
- the size ℓ_{FPZ} of the process zone, in which all fracture dissipative processes (e.g. bond breaking, plasticity, damage) are confined (Fig. 1.b);
- the width ℓ_Δ of the interface, within which the toughness properties vary from G_c^{mat} to G_c^{inc}, with the possible intermediary value G_c^{int} (Fig. 1.c).

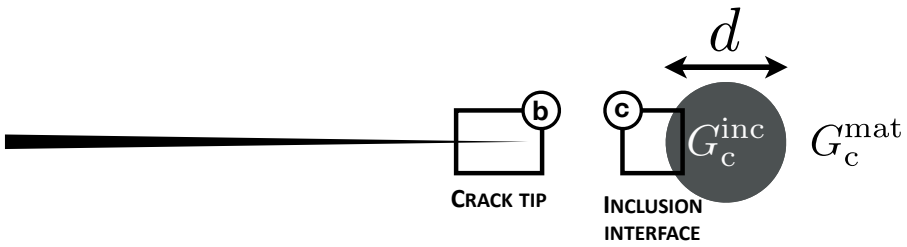

(a) Crack-inclusion interaction

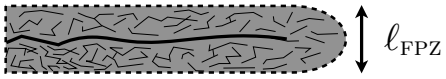

(b) Fracture process zone

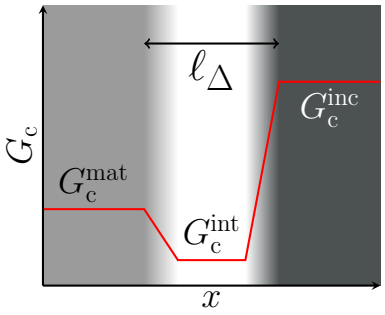

(c) Fracture properties variations

Figure 2: Illustration of the different lengthscales involved during the interaction of a crack with an inclusion : the inclusion size d, the size ℓ_{FPZ} of the process zone, within which all inelastic processes are confined, and the interface width ℓ_Δ, characterizing the size of the transition region between the fracture toughness of the matrix and the one of the inclusion.

Assuming brittle failure, we suppose that the process zone size is much smaller than the inclusion size. In addition, assuming toughness discontinuitiesat the matrix-inclusion interface implies that the interface width is much smaller than the process zone size. Finally using a semi-infinite crack model relies on the assumption that the inclusion size is much smaller than any structural sizes - otherwise effects tied to the specimen dimensions could be observed, as reported by Legrand et al. (2011). To summarize, the following assumptions are made:

$$\ell_\Delta \ll \ell_{FPZ} \ll d \ll L_{struct}. \tag{1}$$

These hypotheses are acceptable for a large range of brittle materials including ceramics, glasses or brittle rocks like limestone.

The proposed description of a typical microstructure of a heterogeneous brittle solid leads to a three-dimensional toughness field $G_c(z, x, y)$. This field markedly differs from those considered in previous three-dimensional perturbative studies (Ramanathan et al., 1997; Barès et al., 2014) which used a stochastic field of fracture energy deriving from a statistical distribution, since we consider here actual microstructures resulting from inclusions with given shape and fracture properties. Also, the perturbations introduced in the set of LEFM equations will not be imposed heuristically but deduced from the actual interaction between the crack and the inclusions. It is worth noticing that the methodology proposed may be applied to any defect geometry provided that the defect boundary and in particular the normal vector to this boundary are unambiguously defined, which may be achieved for instance using level set methods. An example involving prolate spheroidal inclusions will be provided in Sections 5 and 6.

2.2. Calculation of the SIFs along the crack front

2.2.1. Macroscopic loading

We consider a semi-infinite plane crack loaded in mode I through some loading characterized by some load parameter λ corresponding to either some prescribed displacement or some prescribed force. The effects of the loading conditions and the sample geometry are accounted for in our model through the following assumed evolution of the macroscopic ERR G^∞ with the average position x of the crack front:

$$G^\infty(\lambda, x) = \lambda^2 g(x). \tag{2}$$

The "geometrical contribution" $g(x)$ to the value of the ERR may be obtained from analytical solutions or FE simulations. We assume that $g'(x) < 0$, $\forall x$, which warrants stable crack growth, *i.e.* crack arrest under constant loading ($\dot{\lambda} = 0$). Note that it is assumed here that the macroscopic ERR G^∞ is constant along the reference straight crack front (independent of z).

In order to keep the study of the effects of loading conditions and sample geometry as simple as possible, we follow Ponson and Bonamy (2010) and limit our analysis to short propagation distances $x(t) \ll \mathcal{L}$, where $\mathcal{L}$ is a structural length defined from the variations of the function $g(x)$. The loading rate $\dot{\lambda}$ being considered as constant, we get at the first order :

$$G^\infty(\lambda, x) = G^\infty(\lambda_0, 0) + \left.\frac{\partial G^\infty}{\partial \lambda}\right|_{\lambda_0,0} \dot{\lambda} t + \left.\frac{\partial G^\infty}{\partial x}\right|_{\lambda_0,0} x \tag{3}$$

or equivalently:

$$G^\infty(t) = G_0\left(1 + \frac{v_m t - x(t)}{\mathcal{L}}\right) \tag{4}$$

where $G_0 = G^\infty(\lambda_0, x_0 = 0)$ is the initial loading. The structural length $\mathcal{L}$ and the driving velocity v_m are defined by :

$$\mathcal{L} = -G_0 / \left.\frac{\partial G^\infty}{\partial x}\right|_{\lambda_0,0}, \; v_m = -\dot{\lambda} \left.\frac{\partial G^\infty}{\partial \lambda}\right|_{\lambda_0,0} / \left.\frac{\partial G^\infty}{\partial x}\right|_{\lambda_0,0}. \tag{5}$$

After an initial transient phase, the crack propagates at an average (in time) velocity equals to v_m so that G^∞ remains finite during crack propagation (see Eq. (4)).

2.2.2. Perturbative expression of the local SIFs

In a homogeneous material, the semi-infinite crack would undergo stable coplanar propagation at the speed v_m, and the crack front $\mathcal{F}$ would remain straight at the instantaneous position $x(t) = v_\mathrm{m}t$. But material heterogeneities distort the crack front both within the mean fracture plane (crack trapping) and out of it (crack deflection). In the following, we note $f_x(z,t)$ the in-plane perturbation of the crack front, and $f_y(z,t)$ its out-of-plane perturbation. The in-plane perturbation is defined from the reference crack position $x(t)$ (see Fig. 3) chosen so as to satisfy the condition $\langle f_x(z,t)\rangle_z = 0$. With these notations, the coordinates of a point M along the crack front are given by $(z_M, x_M, y_M) = \Big(z, x(t) + f_x(z,t), f_y(z,t)\Big)$.

Assuming quasi-static crack propagation,[1] one can use the formulæ of Gao and Rice (1986) (for the in-plane perturbation of the crack front) and those of Movchan et al. (1998) (for the out-of-plane perturbation of the crack surface) to compute the variations $\Big(\delta K_p\Big)_{p\in\{\mathrm{I,II,III}\}}$ of the SIFs from the reference geometry. At first order in f_x and f_y, the expressions of the SIFs read:

$$\begin{cases} \dfrac{\delta K_\mathrm{I}(z,t)}{K_\mathrm{I}^\infty(t)} = -\dfrac{f_x(z,t)}{2\mathcal{L}} - \dfrac{1}{2\pi}\,\mathrm{PV}\displaystyle\int_{-\infty}^{+\infty}\dfrac{f_x(z,t)-f_x(z',t)}{(z-z')^2}\,dz' \\ \dfrac{\delta K_\mathrm{II}(z,t)}{K_\mathrm{I}^\infty(t)} = \dfrac{1}{2}\dfrac{\partial f_y}{\partial x}(z,t) + \dfrac{2-3\nu}{2-\nu}\dfrac{1}{2\pi}\,\mathrm{PV}\displaystyle\int_{-\infty}^{+\infty}\dfrac{f_y(z,t)-f_y(z',t)}{(z-z')^2}\,dz' \\ \dfrac{\delta K_\mathrm{III}(z,t)}{K_\mathrm{I}^\infty(t)} = -\dfrac{2(1-\nu)^2}{2-\nu}\dfrac{\partial f_y}{\partial z}(z,t) \end{cases} \tag{6}$$

where $K_\mathrm{I}^\infty(t)$ denotes the unperturbed mode I SIF and the symbol PV a Cauchy principal value.

Note that the general expressions of Gao and Rice (1986) and Movchan et al. (1998) have been simplified here in two respects:

- Since the specimen is assumed to be loaded in pure mode I, K_II^∞ and K_III^∞ are equal to zero. Furthermore K_I^∞ is related to G^∞ through the relation $K_\mathrm{I}^\infty = \sqrt{\frac{E}{1-\nu^2}\,G^\infty}$.
- The largest wavelength of the perturbation of the front is assumed to be much smaller than the characteristic structural lengths defined by the loading and the specimen geometry, so one may neglect the terms related to the T-stresses (corresponding to constant terms in the asymptotic expansion of the stresses) and the A-stresses (corresponding to terms proportional to $\sqrt{r}$ in this asymptotic expansion) in the expressions of the variations of the SIFs (Leblond and Ponson, 2016).

From Eq. (6), we notice that :

- Even though the crack is loaded macroscopically in Mode I, local Mode II and Mode III components can arise from out-of-plane distortions of the crack.
- Long-range elastic interactions exist along the crack front through the integral terms. This may lead to collective response of the crack during its propagation in a three-dimensional medium as the behavior of a given point along the front is affected by the evolution of all the other ones.

[1] The crack speed is assumed to be small with respect to the Rayleigh wave speed at any time and any position along the front. This assumption is generally satisfied even in the presence of the micro-instabilities resulting from the depinning of the crack from tough obstacles, as shown in Chopin et al. (2018)

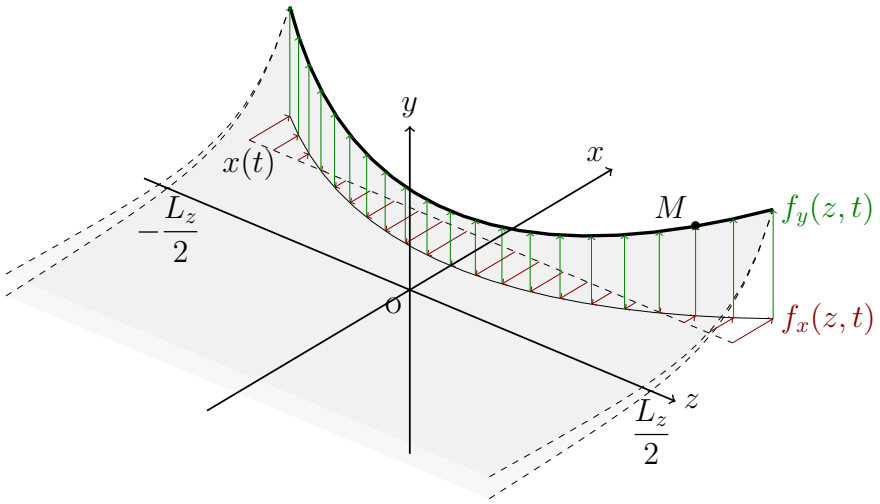

Figure 3: Geometrical perturbations of a semi-infinite planar crack located in $x(t)$. $f_x(z,t)$ and $f_y(z,t)$ represent its in-plane and out-of-plane perturbations, respectively

- There are no terms proportional to f_y in the expression of δK_{I}, and no terms proportional to f_x in the expressions of δK_{II} and δK_{III}, a consequence of the various symmetries of the problem.

Formulæ (6) permit to compute the SIFs $\left(K_{\mathrm{I}}^M, K_{\mathrm{II}}^M, K_{\mathrm{III}}^M\right)$, and thus the ERR G at any location M along the crack front. Since the toughness values along the front and in its vicinity are determined from the position $\left(z, x(t) + f_x(z,t), f_y(z,t)\right)$, there remains only one missing piece in the puzzle, the propagation criterion, which is detailed hereafter.

2.3. The GMERR propagation criterion

2.3.1. Propagation states

During crack propagation, every point along the crack front can be in four different states depicted in Fig. 4:

- **State I**: the point is propagating inside the matrix and may encounter an inclusion (Fig. 4.a and 4.b);
- **State II**: the point has just "landed" on a tough inclusion and is now trapped at its interface with the matrix (Fig. 4.c and 4.d);
- **State III**: after depinning from the matrix-inclusion interface, the crack crosses the inclusion (Fig. 4.e and 4.f);
- **State IV**: after depinning from the matrix-inclusion interface, the crack by-passes the inclusion, thus leaving the original fracture plane (Fig. 4.g and 4.h).

One may distinguish between two types of propagation states. In State i and State iii the point M is in a homogeneous phase; whereas in State ii and State iv, it lies on a interface

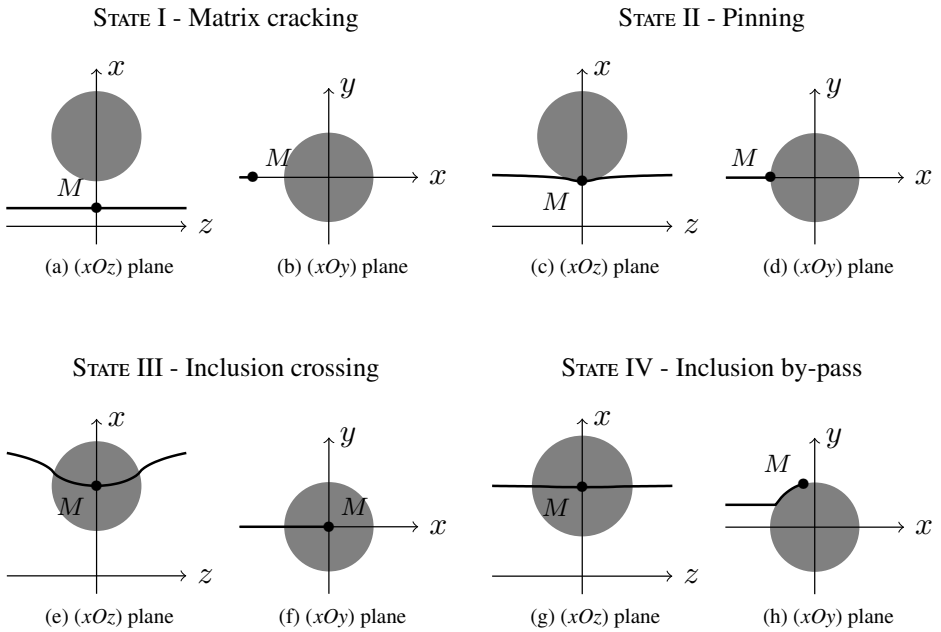

(a) (xOz) plane (b) (xOy) plane (c) (xOz) plane (d) (xOy) plane

(e) (xOz) plane (f) (xOy) plane (g) (xOz) plane (h) (xOy) plane

Figure 4: The four possible states of a point M on a crack front during crack propagation in a heterogeneous medium with toughness discontinuities

between two materials having different toughnesses. The local angular distribution of toughness is here anisotropic.

Standard propagation criteria combine a kinetic law (which may or may not be equivalent to Griffith's criterion (Griffith, 1921)) together with a criterion for crack path prediction, usually chosen among the Maximum Tangential Stress criterion (MTS) (Erdogan and Sih, 1963), the Maximum Energy Release Rate criterion (MERR) (Hussain et al., 1974) or the Principle of Local Symmetry (PLS) (Gol'dstein and Salganik, 1974; Cotterell and Rice, 1980). To deal with heterogeneous materials exhibiting toughness discontinuities, the MERR, suitably generalized to the anisotropic case, is more appropriate as it permits to apply a single criterion to all four states described previously.

2.3.2. Direction criterion

Generally, a point along the front is assumed to propagate within the plane orthogonal to the local tangent to the crack front, as depicted in Fig. 5). Here, we consider instead that each point M on the crack front propagates within the (xMy) plane. This approximation greatly simplifies the numerical procedure and avoid the costly remeshing strategies performed in(Bower and Ortiz, 1990) and (Lazarus, 2003). The errors introduced are of second-order and thus negligible within our first-order perturbation model.

For pedagogical reasons, we shall now comment the application of the criterion first to STATE II and STATE IV, then to STATE I and STATE III.

*Pinning on an interface (*STATE II*).*

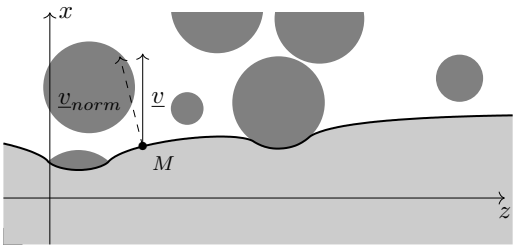

Figure 5: Crack propagation direction: each point M of the crack is considered to propagate within the plane (xMy), along the direction $\underline{v}$ instead of the direction $\underline{v}_{\text{norm}}$ orthogonal to the crack front

Let us first consider a point M on a crack front which has just landed on an inclusion with an attack angle θ_{ini} at a landing height $y_{\text{landing}} = \left(y_p - y^s\right)$, as depicted in Fig. 6. The angle defining the subsequent propagation direction is denoted θ. The angular distribution of toughness is defined as follows:

$$\begin{cases} G_{\text{c}}(\theta) = G_{\text{c}}^{\text{mat}}, \text{ if } \theta \in [-\pi, -\pi + \theta_{\text{tan}}) \cup (\theta_{\text{tan}}, \pi] \\ G_{\text{c}}(\theta) = G_{\text{c}}^{\text{inc}}, \text{ if } \theta \in (-\pi + \theta_{\text{tan}}, \theta_{\text{tan}}) \\ G_{\text{c}}(\theta) = G_{\text{c}}^{\text{int}}, \text{ if } \theta = -\pi + \theta_{\text{tan}} \text{ or } \theta = \theta_{\text{tan}} \end{cases} \tag{7}$$

For instance, the variations of G_{c} versus the angle θ defining the propagation direction are shown in Fig. 8.a for $\theta_{\text{tan}} = 45°$, $G_{\text{c}}^{\text{inc}} = 1.4\, G_{\text{c}}^{\text{mat}}$ and $G_{\text{c}}^{\text{int}} = 0.8\, G_{\text{c}}^{\text{mat}}$. This distribution of toughness is clearly anisotropic. Unlike the PLS which applies to isotropic materials only, the MERR criterion is basically applicable to anisotropic media as well (Gurtin and Podio-Guidugli, 1998; Hakim and Karma, 2005; Chambolle et al., 2009). We therefore adopt the following criterion:

Propagation occurs in the direction θ such that $(G - G_{\text{c}})(\theta)$ be globally maximal. (8)

This criterion, called the Generalized Maximum Energy Release Rate (GMERR) in the sequel, will also be applied when the point of the crack front considered is within the matrix or inside the inclusion.

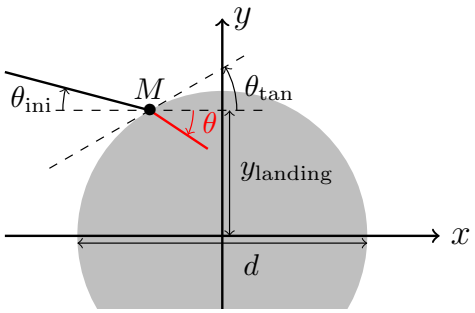

Figure 6: Crack landing on an inclusion with an attack angle θ_{ini} at a landing height y_{landing} corresponding to a local tangent angle θ_{tan}.

The GMERR criterion may equivalently be expressed in a variational form, see Francfort and Marigo (1998). Indeed, maximizing $G - G_{\text{c}}$ is equivalent to minimizing the sum of the

elastic (volume) energy and the fracture (surface) energy. This criterion has recently been verified experimentally through tearing tests of brittle polymeric thin sheets with weakly (Ibarra et al., 2016) and strongly (Takei et al., 2013) anisotropic fracture properties. It has also been confirmed numerically through anisotropic phase-field simulations (Hakim and Karma, 2005, 2009; Bleyer and Alessi, 2018; Li and Maurini, 2019)

Since the point M lies on the interface between two materials with identical elastic properties, one may apply the so-called Amestoy-Leblond formulæ (see for instance Leblond (1999)). These formulæ link the local SIFs, $\underline{\mathbf{K}}^*$, just after an arbitrary kink to those, $\underline{\mathbf{K}}$, just before it, see Fig. 7. They read:

$$\underline{\mathbf{K}}^* = \underline{\underline{\mathbf{F}}}(\alpha) . \underline{\mathbf{K}} \tag{9}$$

where $\underline{\underline{\mathbf{F}}} = \left(F_{i,j}\right)$ is a universal operator depending only on the (arbitrary) kink angle α. These formulæ show that whatever the geometry and the loading, the SIFs right after a kink depend only on those before the kink and the angle defining this kink. It is also worth noting that $F_{\mathrm{I,III}} = F_{\mathrm{III,I}} = 0$, which evidences the decoupling of the plane and anti-plane loading modes.

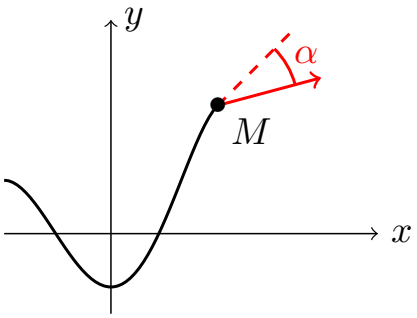

Figure 7: Schematics of a crack kinking situation where an initial crack suddenly propagates with an arbitrary large kink α

We use these formuæ to obtain the angular distribution of the SIFs at the tip of an infinitesimal extension in the direction defined by the angle θ from the values of the SIFs K_{I}^M, K_{II}^M and K_{III}^M before the kink :

$$\begin{cases} K_{\mathrm{I}}(\theta) = F_{\mathrm{I,I}}(\theta - \theta_{\mathrm{ini}}) K_{\mathrm{I}}^M + F_{\mathrm{I,II}}(\theta - \theta_{\mathrm{ini}}) K_{\mathrm{II}}^M \\ K_{\mathrm{II}}(\theta) = F_{\mathrm{II,I}}(\theta - \theta_{\mathrm{ini}}) K_{\mathrm{I}}^M + F_{\mathrm{II,II}}(\theta - \theta_{\mathrm{ini}}) K_{\mathrm{II}}^M \\ K_{\mathrm{III}}(\theta) = F_{\mathrm{III,III}}(\theta - \theta_{\mathrm{ini}}) K_{\mathrm{III}}^M \end{cases} \tag{10}$$

The values of the SIFs K_{I}^M, K_{II}^M and K_{III}^M are provided by the perturbative framework presented above, see Eq. (6):

$$\begin{cases} K_{\mathrm{I}}^M = K_{\mathrm{I}}^\infty(t) + \delta K_{\mathrm{I}}(z,t) \\ K_{\mathrm{I}}^M = \delta K_{\mathrm{II}}(z,t) \\ K_{\mathrm{I}}^M = \delta K_{\mathrm{III}}(z,t) \end{cases} \tag{11}$$

.

By combining Eq. (11) with Irwin's formula, we get :

$$G(\theta) = \frac{1-\nu^2}{E}\left(K_{\mathrm{I}}^2(\theta) + K_{\mathrm{II}}^2(\theta)\right) \tag{12}$$

where we have eliminated the Mode III contribution, which is of second order in the perturbation since $K_{\mathrm{III}}(\theta)$ is itself of first order. An example of the angular distribution of the ERR thus defined is given in Fig. 8.b.

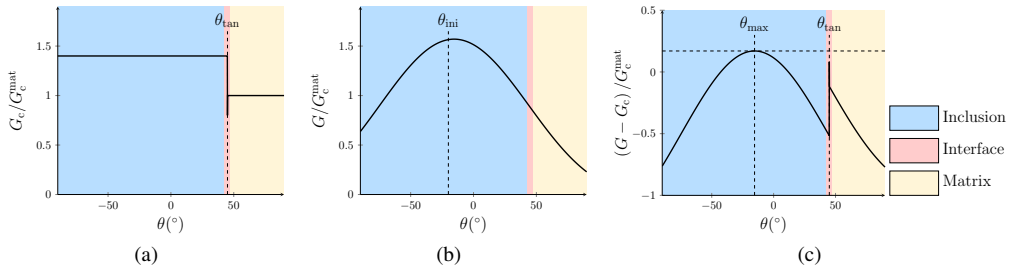

Figure 8: Application of the GMERR direction criterion: (a) Variations of the toughness G_c, (b) the ERR G and (c) their difference $G - G_c$ with the potential propagation direction θ, for the parameter values $\theta_{\mathrm{tan}} = 45°$, $\theta_{\mathrm{ini}} = -20°$, $G_c^{\mathrm{inc}} = 1.4\,G_c^{\mathrm{mat}}$ and $G_c^{\mathrm{int}} = 0.8\,G_c^{\mathrm{mat}}$, $K_{\mathrm{I}}^M = 1.25K_{I,c}^{\mathrm{mat}}$ and $K_{\mathrm{II}}^M = -0.05K_{I,c}^{\mathrm{mat}}$.

We then obtain the difference $G - G_c$ as a function of the angle θ defining the propagation direction that is shown in Fig. 8.c. In practice, it not necessary to compute $G - G_c$ in all directions, but only along the tangent θ_{tan} and along the direction θ_{max} that maximizes G, as shown in Appendix B.

Application of the GMERR criterion finally amounts to determining the propagation direction θ satisfying the following conditions:

$$\theta \in \{\theta_{\mathrm{tan}}, \theta_{\mathrm{max}}\} \text{ and } (G - G_c)(\theta) \text{ is maximum.} \tag{13}$$

The physical implications of such a criterion on the crack trajectory will be studied in detail in Section 4.1.

*Propagation along an interface matrix/inclusion (*State IV*).*

When the point M is propagating along an interface between the matrix and the inclusion, we apply the same criterion as before with the sole difference that $\theta_{\mathrm{ini}} = \theta_{\mathrm{tan}}$ since kinking has already occurred. Note that the crack can remain on the interface, stop by-passing the inclusion and cross it, or leave the interface and go back to the matrix.

*Propagation within homogeneous phases (*State I & III*).*

When a point M is either in the matrix or crossing an inclusion, the angular distribution of toughness $G_c(\theta)$ is isotropic so that the PLS is applicable. However, since the MERR and the PLS are in practice almost equivalent for the small kink angles encountered in the homogeneous phases (Amestoy and Leblond, 1992), we retain the GMERR criterion.

2.3.3. Kinetic law

The last missing ingredient is the kinetic law that relates the local crack velocity v to G and G_c. For brittle materials, this kinetic law can be derived from Griffith (1921)'s criterion by accounting for the variations of the toughness with the crack speed (Kolvin et al., 2015; Chopin et al., 2018).

All points of the crack front are assumed to follow Griffith's criterion :

$$G = G_c(v) \tag{14}$$

where G does not depend on crack speed v under the hypothesis of quasi-static propagation. We then postulate that the toughness is a given function of the crack speed, $G_c = G_c(v)$. Depending on the material, the function $G_c(v)$ may take different forms. Its linearization around the mean crack velocity v_m provides a linear kinetic law:

$$G = G_c(v) = G_c(v_m)\left(1 + \frac{v - v_m}{v_0}\right) \quad (\text{for } v > 0) \quad \Leftrightarrow \quad v = \left[v_m + v_0 \frac{G - G_c(v_m)}{G_c(v_m)}\right]^+ \tag{15}$$

where $v_0 = G_c(v_m) \Big/ \left.\frac{\partial G_c}{\partial v}\right|_{v_m}$ is a characteristic velocity of the material emerging from the rate-dependency of its toughness and $[\cdot]^+$ the positive part function. This equation of motion has been largely used in the literature (see for example (Gao and Rice, 1989; Ramanathan et al., 1997; Ponson and Bonamy, 2010)) and was recently shown to capture quantitatively the relaxation dynamics of a crack depinning from a single obstacle (Chopin et al., 2018).

2.4. Validity range of the perturbative approach

The perturbative procedure used requires $\left|\frac{\partial f_x}{\partial z}\right| \ll 1$, $\left|\frac{\partial f_y}{\partial z}\right| \ll 1$, $\left|\frac{\partial f_y}{\partial x}\right| \ll 1$, which raises the issue of the validity range of our approach. Gao and Rice (1989) studied the validity range of the first-order perturbation for coplanar crack propagation. They showed that for inclusions with $G_c^{inc} \simeq 4\, G_c^{mat}$, the perturbative approach gives accurate results when compared to boundary elements simulations. Above this toughness level, the results of the perturbative framework are no more quantitatively correct and can even be qualitatively wrong. We thus limit our study to such toughness levels, ensuring the condition $\left|\frac{\partial f_x}{\partial z}\right| \ll 1$.

Regarding the out-of-plane perturbations of the crack, Eq. (6) provides a good estimate of the SIFs even for large values of the slope $\theta = \arctan\left(\frac{\partial f_y}{\partial x}\right)$, *provided* it is corrected through use of Amestoy-Leblond's formulæ (Amestoy and Leblond, 1992; Leblond, 1999) that provide the SIFs just after an abrupt, arbitrary change of direction of the crack. The necessary procedure of correction is described in Appendix A. This procedure permits to handle the large slope which may arise during the by-pass of inclusions. It is also explained in the same Appendix that even with the procedure of correction, the mode III contribution is of second-order in the expression of the ERR G, due to the decoupling of the anti-plane shear mode with respect to the tensile and plane shear modes in Amestoy-Leblond's formulæ. Neglect of this contribution implies that the derivative $\frac{\partial f_y}{\partial z}$ plays no role in the model.

3. Numerical implementation

The toughness G_c and the ERR G are the central quantities in our model, so they need to be computed accurately and efficiently along the crack front at every time step. Section 3.1 presents the method employed to generate 3D microstructures with heterogeneous fracture properties, leading to the calculation of G_c, while Section 3.2 describes the procedure used to compute the SIFs $\left(K_p\right)$ and subsequently G along the front.

3.1. Microstructure generation

Random isotropic non-overlapping microstructures are built using the so-called random sequential addition algorithm proposed by Widom (1966) which consists in placing randomly and sequentially non-overlapping spheres in a fixed volume. This procedure works efficiently for low densities (up to 30%) or highly polydisperse microstructures. For higher densities and low diameter dispersion levels, we use the algorithm proposed by Delarue and Jeulin (2011), which consists in starting from a dense ordered cubic closed-packing of inclusions, and then randomizing it by randomly deleting or moving some of them. These efficient methods permit to generate large-scale isotropic disordered microstructures (typically 10^6 inclusions) within short computation times. Some examples of the generated microstructures are shown in Fig. 9.

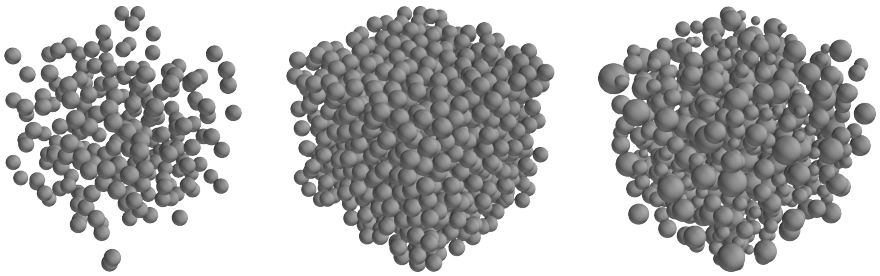

(a) (b) (c)

Figure 9: Different microstructures considered in our model: (a) monodisperse at 20% density (a), (b) monodisperse at 50% density (c) and polydisperse at 30% density.

3.2. Crack advance procedure

3.2.1. Crack front discretization

The crack front is discretized in N points $(M_i)_{i\in[1,N]}$ separated by a uniform distance $\Delta z = \frac{L_z}{N}$ as depicted in Fig. 10. The positions $\left(x + f_x^i, f_y^i, z_i\right)$ of these points are tracked at each time step, subsequent positions being inferred from the instantaneous and local velocity vector $\underline{v}^i$ oriented in the direction $\theta^i = \arctan\left(\frac{\partial f_y^i}{\partial x}\right)$ in the (xM_iy)-plane.

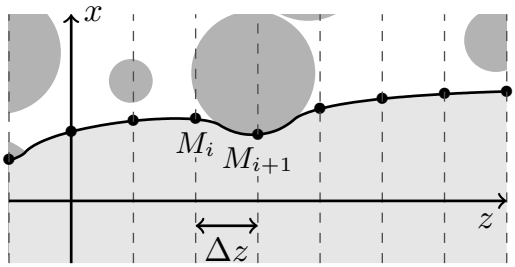

Figure 10: Crack front discretization with a spatial step Δz

3.2.2. Accelerated computation of the SIFs

The fast computation of the local SIFs along the front is a key element of the numerical implementation. Equations (6) relate the distribution of the SIFs to the geometrical perturbations of the front, and involve integrals along the whole crack front. Such integrals are computationally costly as their computational time grows as $O\left(N^2\right)$, where N is the number of discretization points along the front. However, if one assumes that the material is *periodic* along the crack front direction, these non-local terms take a simple local form in Fourier's space. Indeed, if we define the z-Fourier transform $\hat{\phi}$ of an arbitrary real function ϕ by the equivalent formulæ :

$$\hat{\phi}(k,t) = \int_{-\infty}^{+\infty} \phi(z,t)\, e^{-ikz} dz \Leftrightarrow \phi(z,t) = \frac{1}{2\pi} \int_{-\infty}^{+\infty} \hat{\phi}(k,t)\, e^{+ikz} dk \tag{16}$$

then the operator defined by the integrals along the crack front takes the following form in Fourier's space :

$$Cf(z,t) = \mathrm{PV} \int_{-\infty}^{+\infty} \frac{f(z,t) - f(z',t)}{(z-z')^2}\, dz' \quad \Leftrightarrow \quad \widehat{Cf}(k,t) = |k|\pi \hat{f}(k,t)\,. \tag{17}$$

This property allows to compute efficiently the non-local contributions to the SIFs perturbations through direct and inverse Fast Fourier Transforms (FFTs), thus reducing the computational cost to $O(N\log N)$. To optimize the FFT algorithm, the number of crack front points $N = 2^p$ is generally chosen as a power of 2.

3.2.3. Numerical scheme

The computation of the crack evolution employs an explicit scheme in time, that predicts the configuration of the front at time $t + \Delta t$ from that at time t. Each point along the crack front is characterized by the parameters $x(t)$, $f_x(z,t)$, $f_y(z,t)$ and $\theta(z,t)$, from which the subsequent position is deduced.[2] First, the variations $G_c(z,t)$ of toughness along the front are deduced from the location of the crack front within the heterogeneous microstructure. Second, the instantaneous macroscopic loading $G^\infty(t)$ is computed from the time t and the average position $x(t)$ using Eq. (4). The perturbed SIFs $\left(K_p\right)$ are then inferred from the crack front deformations using the formula provided in Appendix A, with the numerical method described in Section 3.2.2. Finally, the direction of the velocity vector $\underline{v}(z,t)$ is determined from the GMERR criterion of Eq. (13), and its norm is computed from the kinetic law of Eq. (15). Convergence criteria explained below set the time-step size Δt, and the simulation runs until the whole microstructured medium is broken.

3.3. Convergence criteria

Explicit numerical schemes are often preferred to implicit schemes since they are easier to implement. One of their major drawbacks is that they require a small time step Δt to ensure numerical stability and control numerical errors. We examine here the possible sources of numerical instabilities and propose a convergence criterion adapted from a Courant-Friedrichs-Lewy condition.

[2]Note that knowledge of the past configurations of the front is not necessary, as the fully non-local terms in the expressions of the perturbed SIFs (Movchan et al., 1998), that consist in integrals over the full fracture surface, can be neglected, as argued in Section 2.2.2

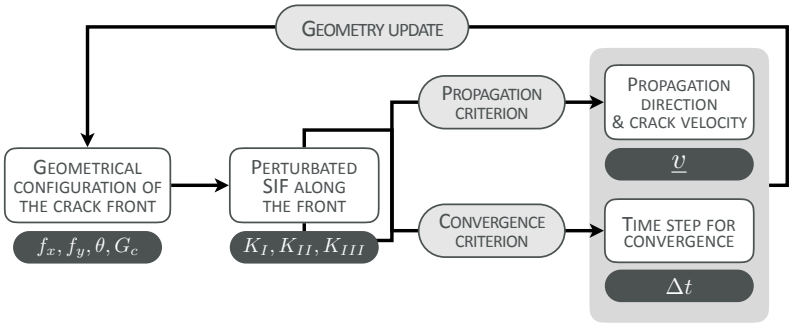

Figure 11: Explicit numerical scheme employed for the prediction of the crack evolution

3.3.1. Absolute convergence

The explicit scheme employed in our computations may lead to numerical artifacts in the form of oscillations of the SIFs along the front. These oscillations result from the toughness discontinuities considered in the modelling of the microstructure, as illustrated in (Fig. 12.a). Indeed when a crack lands on some inclusion, the toughness experienced by the point in contact with the inclusion increases discontinuously, leading to the sudden arrest of this point. However, as the neighboring points of the crack front keep moving (Fig. 12.b), oscillations in the non-local contribution of the expressions of the perturbed SIFs may appear (Fig. 12.c).

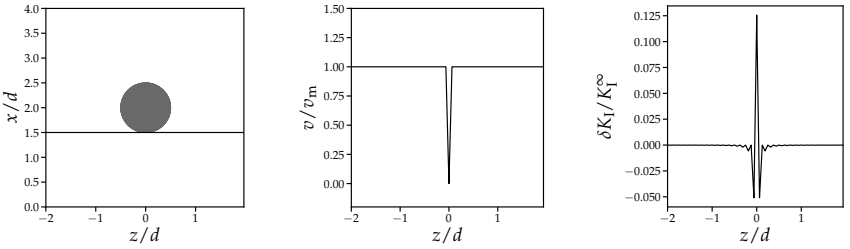

(a) Crack position (b) Crack velocity (c) Long-range perturbation of the SIF

Figure 12: Oscillations induced on long-range interactions during pinning of a crack front on an inclusion

Numerical schemes used by other authors (Bower and Ortiz, 1990; Lazarus, 2003; Ponson and Pindra, 2017) avoid this numerical instability by imposing a maximum value to the *crack growth increment* during each time interval. Here, we prefer to impose a maximum *time-step* Δt_{conv} adapted to our explicit scheme, since a time-step criterion ensures convergence, irrespective of the inclusion properties. The maximum time-step Δt_{conv} is determined from the analysis of the *coplanar* crack propagation problem, which is governed by the following dimensionless equation (Ponson and Pindra, 2017) :

$$\frac{1}{v_0}\frac{\partial f_x}{\partial t}(z,t) = -\frac{1}{\pi}\,\text{PV}\int_{-\infty}^{+\infty}\frac{f(z,t)-f(z',t)}{(z-z')^2}\,dz' + \eta_c\left(z, x+f_x(z,t)\right) \tag{18}$$

where the function η_c describes the relative variations of toughness within the propagation plane.

Upon discretization along the z-axis with a spatial step Δz, the integral approximately becomes:

$$-\frac{1}{\pi}\,\mathrm{PV}\int_{-\infty}^{+\infty}\frac{f(z,t)-f(z',t)}{(z-z')^2}\,dz' \simeq -\frac{1}{\pi}\left(\int_{-\infty}^{z-\Delta z}+\int_{z+\Delta z}^{+\infty}\right)\frac{f(z,t)-f(z',t)}{(z-z')^2}\,dz' + \frac{\Delta z}{\pi}\frac{\partial^2 f}{\partial z^2}(z,t) \tag{19}$$

Since the numerical instabilities are caused by the curvature term, a Courant-Friedrichs-Lewy convergence condition:

$$\Delta t_{\mathrm{conv}} = \alpha\, v_0\, \Delta z, \tag{20}$$

where the constant α is set to 0.2, is employed. This type of condition is widely and successfully used in numerical simulations of diffusion problems. Examples of simulations of crack propagation with $\Delta t_{\mathrm{step}} = \Delta t_{\mathrm{conv}}$ and $\Delta t_{\mathrm{step}} > \Delta t_{\mathrm{conv}}$ are given in Fig. 13.

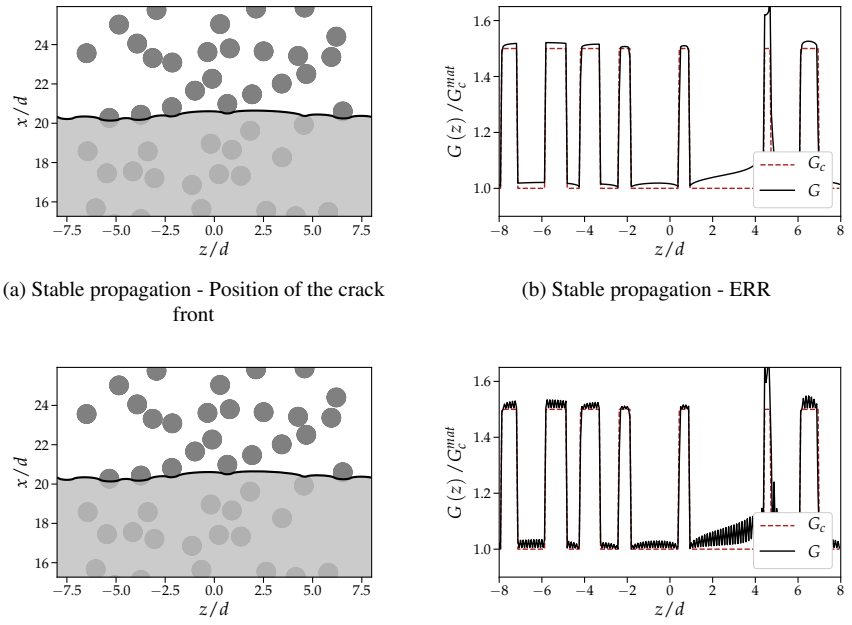

(a) Stable propagation - Position of the crack front

(b) Stable propagation - ERR

(c) Unstable propagation - Position of the crack front

(d) Unstable propagation - ERR

Figure 13: (a) & (b) Non-oscillatory behaviour for $\Delta t_{\mathrm{step}} = \Delta t_{\mathrm{conv}}$; (c) & (d) oscillatory behaviour for $\Delta t_{\mathrm{step}} > \Delta t_{\mathrm{conv}}$.

3.3.2. Other restraining conditions

Other conditions are imposed to the numerical scheme in order to ensure a realistic and accurate modeling of the crack evolution:

- **Interaction with microstructure** – We make sure that no point on the crack front crosses a toughness discontinuity during a time-interval, as its behavior at such interfaces largely controls the interaction mechanism between the crack and the inclusion. As a result, the

time step may be adjusted to a value $\Delta t_{\text{inter}} < \Delta t_{\text{conv}}$ to ensure that the crack lands exactly on the interface;

- **Maximum advance** – We introduce a maximum value $\Delta x_{\max} = \Delta z/5$ of the incremental crack advance, in order to avoid sudden variations of the non-local contributions to the SIFs perturbations (see Section 3.3.1). This introduces a maximum time step $\Delta t_{\text{advance}} = \frac{\Delta x_{\max}}{\max_{\mathcal{F}} v}$ which is generally much larger than Δt_{conv};

- **Maximum load variations** – A maximum value $\Delta G_{\max}$ of the load variation between subsequent time steps is introduced to avoid sudden drops of G^{∞} during the depinning phases. According to Eq. (4), this leads to an additional time scale $\Delta t_{\text{loading}} = \Delta G_{\max} \mathcal{L}/v_{\text{m}}$.

During each time interval, the time-step Δt is chosen as the smallest of those defined previously:

$$\Delta t = \min\left(\Delta t_{\text{conv}}, \Delta t_{\text{inter}}, \Delta t_{\text{advance}}, \Delta t_{\text{loading}}\right). \tag{21}$$

Given that the crack propagates along a distance L_x at an average velocity v_m and that the average time step Δt scales as $\Delta z \sim 1/N$ (see Eq. (21)), the simulation requires $M \sim N$ time steps computed in a time proportional to $N\log N$ to complete. The computational complexity of the proposed algorithm is in $O\left(N^2 \log N\right)$.

3.4. Computational performance

The numerical method presented in this paper, based on approximate analytical expressions of the SIFs, permits an efficient computation of quantities of interest like the ERR, using only a 1D discretization of the crack front. As no discretization of the (2D) crack surface, or the entire (3D) body, is required, simulations of crack propagation in heterogeneous media including as many as 10^6 inclusions requires only a few hours using a single core computer. With such a numerical performance, fully 3D fracture simulations of very large specimens can be achieved, as examplified in Fig. 14 and Fig. 15. However the detailed investigation of the effective fracture properties of *disordered* brittle solids is left for future works, and we shall focus in the sequel on seemingly simpler, *periodic* microstructures with only a few inclusions per period.

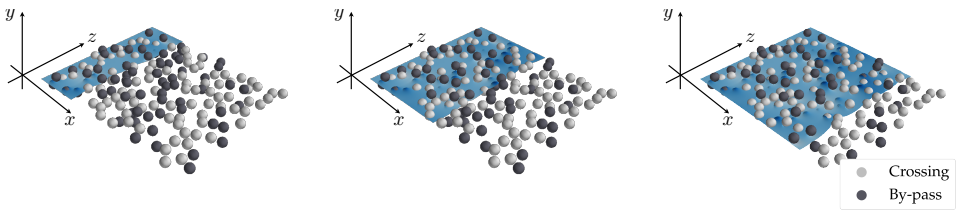

Figure 14: 3D fracture simulations of medium-sized specimens with disordered microstructures illustrating the interaction mechanisms modelled in the newly developed numerical method : crack surface after propagation through a matrix with randomly distributed tough inclusions, that have either been by-passed (dark grey) or crossed (light grey). The computation takes approximately one minute on a single core computer.

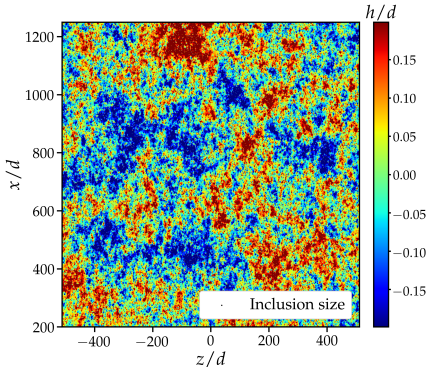

Figure 15: 3D fracture simulations of large-scale specimens with disordered microstructures illustrating the computational performance of the newly developed numerical method. This fracture surface topography characterized by its height map $h(x, y)$, normalized by the inclusion diameter d, results from the interaction of the crack with about 10^6 tough inclusions. The computation takes less than one hour on a single core computer.

4. Inclusion by-pass, a damper of material toughening through crack trapping

4.1. Crack trajectory prediction : competition between by-pass and crossing of inclusions

As is evident in Fig. 14, the competition between crossing and by-pass of inclusions controls the crack trajectory, and so ultimately the effective fracture properties of the heterogeneous medium, as will be discussed in Section 4.2. We start by investigating the mechanisms of interaction of a crack front with a periodic array of tough inclusions, by considering periodic media containing a single inclusion of diameter $d = L_z/4$ per period, with a spatial discretization step $\Delta z = d/32$. As mentioned above, the analysis relies on the GMERR criterion of Eq. (13), that compares the rate G of elastic energy released with the rate of energy G_c dissipated during fracture along the different possible propagation directions.

When the crack front lands on a spheroidal inclusion, two possible propagation mechanisms are in competition: either the crack by-passes the inclusion by propagating along the interface (Fig. 16.a), or it crosses the inclusion by remaining within the mean fracture plane (Fig. 17.a). To by-pass the obstacle, the crack must kink from its initial direction of propagation. As far as the ERR G is concerned, this kink is detrimental since this ERR is maximal along the mean fracture plane, and decreases when the kink angle increases (see Fig. 16.c). Yet, as far as the fracture energy G_c is concerned, kinking allows the crack to select a more favorable path since $G_c^{\text{inc}} \geq G_c^{\text{mat}} \geq G_c^{\text{int}}$ (see Fig. 16.c).

We choose three simple examples to qualitatively illustrate this competition in absence of weak interface, $G_c^{\text{int}} = G_c^{\text{mat}}$:

1. in the first example, the crack lands halfway between the equatorial plane and the top of an inclusion twice tougher than the matrix, $G_c^{\text{inc}} = 2\,G_c^{\text{mat}}$, Fig. 16.a. We denote $\theta_{\text{tan}} = 60°$ the angle between the current propagation direction and the matrix-inclusion interface for the central region of the front (see Fig. 6 with $\theta_{\text{ini}} = 0$ in the present case). As shown in Fig. 16.c, where the normalized net driving force $(G-G_c)/G_c^{\text{mat}}$ is represented as a function of the kink angle θ, the drop of G is smaller than the gain in fracture energy along θ_{tan}, so the crack by-passes the inclusion.

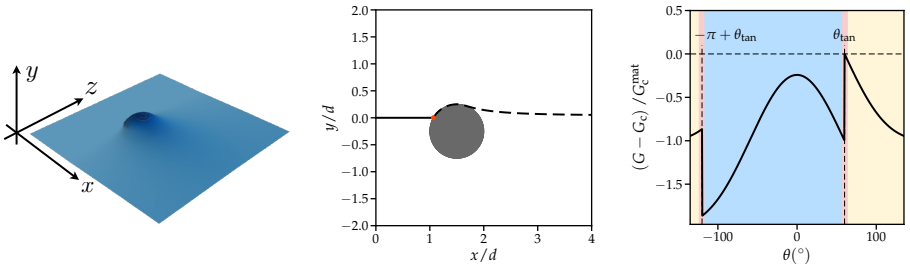

(a) (b) (c)

Figure 16: (a) By-pass mechanism during the trapping of a crack front by a tough spherical inclusion with $G_c^{inc} = 2\,G_c^{mat}$; (b) trajectory of the point of the crack front located in $z = L_z/2$; (c) application of the GMERR criterion of Eq. (13) in $z = L_z/2$; the normalized net driving force is represented as a function of the kink angle at the onset of depinning.

2. Consider now that the crack lands on the equatorial plane (xOz) of the same inclusion, as shown in Fig. 17.b. The kink angle required to by-pass the inclusion is then $\theta_{tan} = 90°$, so that the associated drop of G is significantly larger than in the previous case (Fig. 17.b); this explains here why the crack crosses the tough inclusion rather than than by-passes it.

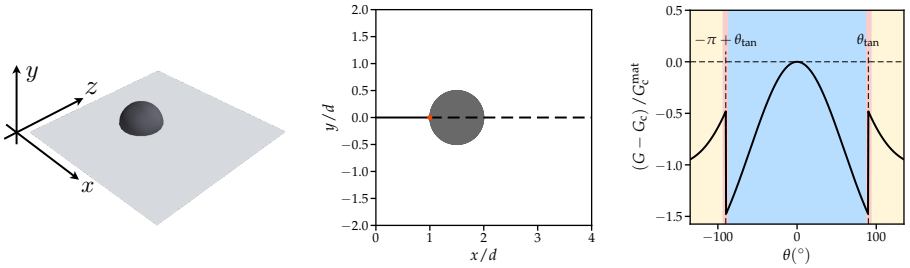

(a) (b) (c)

Figure 17: (a) Crossing mechanism during the trapping of a crack front by a tough spherical inclusion with $G_c^{inc} = 2\,G_c^{mat}$; (b) trajectory of the point of the crack front located at $z = L_z/2$; (c) application of the GMERR criterion of Eq. (13) in $z = L_z/2$; the normalized net driving force is represented as a function of the kink angle at the onset of depinning.

3. In the limit case of an infinitely tough inclusion, it is clear that the crack cannot remain trapped as the external loading is increased further and further, so the inclusion *must* be by-passed, whatever the landing position of the crack front. Thus we expect existence of a critical toughness above which *all* inclusions are by-passed. In Fig. 18, we can see that such a systematic by-pass is already achieved for an inclusion toughness $G_c^{inc} = 4\,G_c^{mat}$.

In general, the competition between crossing and by-pass of a given inclusion is governed by the GMERR criterion, that can be expressed explicitly thanks to Amestoy-Leblond's formulæ of Eq. (10) which provide the value of G after the kink as a function of the SIFs prior to kinking and the kink angle. In our simulations, the SIFs before the kink are computed from the pertubative LEFM formulæ of Eq. (6), which take into account three-dimensional effects due to interactions between different regions of the crack front. Thus the ability of a tough inclusion

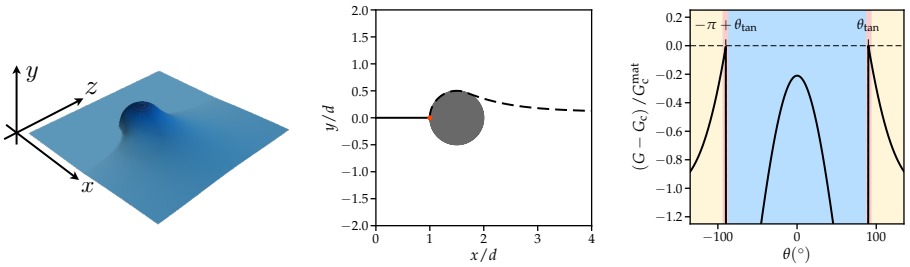

(a) 3D view (b) (x0y) plane (c) $(G - G_c)_{\max}$

Figure 18: (a) By-pass mechanism during the trapping of a crack by a very tough spherical inclusion with $G_c^{\mathrm{inc}} = 4\,G_c^{\mathrm{mat}}$; (b) trajectory of the point of the crack front located at $z = L_z/2$; (c) application of the GMERR criterion of Eq. (13) in $z = L_z/2$; the normalized net driving force is represented as a function of the kink angle at the onset of depinning.

to efficiently trap a crack front results from the complex coupling between the in-plane bowing mode of deformation and the subsequent out-of-plane deviation of the front during the possible by-pass.

4.1.1. A two-dimensional analysis of the GMERR criterion for a cylindrical inclusion

To analyze this mechanism, we start by neglecting the three-dimensional effects due to the variation of f_x and f_y along the crack front and consider a semi-infinite crack landing on an infinite cylindrical inclusion, as illustrated in Fig. 19. We will subsequently compare the results of our numerical simulations with this two-dimensional theoretical analysis in which the SIFs are constant along the front.

Let us assume that the inclusion toughness is G_c^{inc} and the interface toughness G_c^{int}. The initially straight crack lands on the inclusion with an angle θ_{ini}, at a height y_{landing}, at some point on the interface where the tangent angle to the inclusion boundary is $\theta_{\tan}$. This tangent angle is linked to the other parameters through the relation:

$$\theta_{\tan} = \arctan\left(\frac{\sqrt{\left(\frac{d}{2}\right)^2 - y_{\mathrm{landing}}^2}}{y_{\mathrm{landing}}}\right). \tag{22}$$

In order to capture the effect of a mode II component that may result from out-of-plane perturbations of the crack line, we assume that the crack is loaded under mixed mode I+II and we note $\rho_{\mathrm{II}} = K_{\mathrm{II}}/K_{\mathrm{I}}$. As shown in Section 2.3, two directions of crack propagation only need be considered: the direction $\theta_{\max}$ lying within the inclusion and maximizing G, and the by-pass direction $\theta_{\tan}$. According to Amestoy-Leblond's formulæ, the ERR in the direction $\theta_{\max}$ is given by :

$$G_{\mathrm{cross}} = \frac{1-\nu^2}{E} K_{\mathrm{I}}^2 \left[\left(F_{\mathrm{I,I}}(\alpha_{\max}) + F_{\mathrm{I,II}}(\alpha_{\max})\rho_{\mathrm{II}}\right)^2 + \left(F_{\mathrm{II,I}}(\alpha_{\max}) + F_{\mathrm{II,II}}(\alpha_{\max})\rho_{\mathrm{II}}\right)^2 \right] \tag{23}$$

where $\alpha_{\max} = \theta_{\max} - \theta_{\mathrm{ini}}$ is the kink angle in the direction that maximizes G. Similarly, the ERR for the by-pass scenario is provided by :

$$G_{\tan} = \frac{1-\nu^2}{E} K_{\mathrm{I}}^2 \left[\left(F_{\mathrm{I,I}}(\alpha_{\tan}) + F_{\mathrm{I,II}}(\alpha_{\tan})\rho_{\mathrm{II}}\right)^2 + \left(F_{\mathrm{II,I}}(\alpha_{\tan}) + F_{\mathrm{II,II}}(\alpha_{\tan})\rho_{\mathrm{II}}\right)^2 \right]. \tag{24}$$

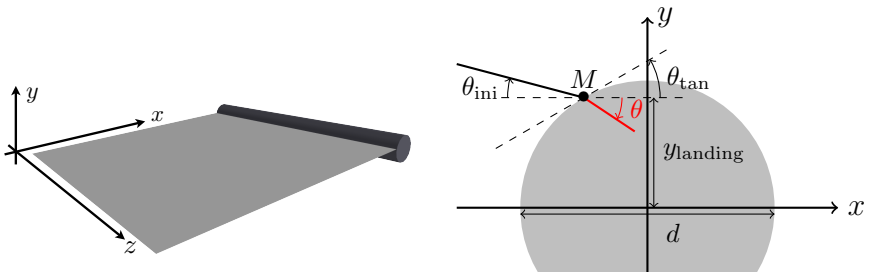

(a) 3D view (b) Plane (xOy)

Figure 19: Two-dimensional analysis of the crossing/by-pass transition: (a) The 2D approximation consists in replacing the spherical inclusion through a cylindrical obstacle invariant in the direction of the crack front; (b) the crack lands with an angle θ_{ini} at a height y_{landing}, and may by-pass the inclusion upwards or downwards.

Now gradually lower the inclusion toughness from infinity to the matrix toughness. At the crossing/by-pass transition, the following equalities must hold:

$$G_{\text{c}}^{\text{inc}} = G_{\text{cross}} \quad , \quad G_{\text{tan}} = G_{\text{c}}^{\text{int}} \tag{25}$$

which leads to :

$$\frac{G_{\text{c}}^{\text{inc}}}{G_{\text{c}}^{\text{int}}} = \frac{G_{\text{cross}}}{G_{\text{tan}}} = \frac{\left(F_{\text{I,I}}\left(\alpha_{\max}\right) + F_{\text{I,II}}\left(\alpha_{\max}\right)\rho_{\text{II}}\right)^2 + \left(F_{\text{II,I}}\left(\alpha_{\max}\right) + F_{\text{II,II}}\left(\alpha_{\max}\right)\rho_{\text{II}}\right)^2}{\left(F_{\text{I,I}}\left(\alpha_{\tan}\right) + F_{\text{I,II}}\left(\alpha_{\tan}\right)\rho_{\text{II}}\right)^2 + \left(F_{\text{II,I}}\left(\alpha_{\tan}\right) + F_{\text{II,II}}\left(\alpha_{\tan}\right)\rho_{\text{II}}\right)^2} ? \tag{26}$$

Specializing this equation to the simpler situation where $\theta_{\text{ini}} = 0$ and $\rho_{\text{II}} = 0$, we obtain the critical toughness ratio at the crossing/by-pass transition :

$$\left[\frac{G_{\text{c}}^{\text{inc}}}{G_{\text{c}}^{\text{int}}}\right]_{\text{crit}} = \frac{1}{F_{\text{I,I}}\left(\theta_{\tan}\right)^2 + F_{\text{II,I}}\left(\theta_{\tan}\right)^2}. \tag{27}$$

Together with Eq. (22), Eq. (27) allows us to draw phase diagrams of the type shown in Fig. 20, where the depinning mechanism (crossing vs by-pass) is easily identified from the value of the toughness ratio $G_{\text{c}}^{\text{inc}}/G_{\text{c}}^{\text{mat}}$ and the relative landing height y_{landing}/d. Several comments are in order here:

- An energetic competition takes place between crossing and by-pass, governed by the inclusion toughness and the magnitude of the kink angle required for by-pass. The theory of LEFM is able to quantitatively predict this competition thanks to Amestoy-Leblond's formulæ;
- In the absence of mode II ($K_{\text{II}} = 0$) and for an attack angle $\theta_{\text{ini}} = 0$, the theoretically predicted upward and downward by-pass regions are symmetric with respect to the horizontal axis $y_{\text{landing}} = 0$. This is because the depinning mechanisms are identical upwards and downwards for a given value of $\left|y_{\text{landing}}\right|/d$. Note also if the crack lands on the upper (resp. lower) half of the inclusion, only an upward (resp. downward) by-pass is possible.
- The critical toughness ratio beyond which the inclusion is systematically by-passed can be deduced from consideration of the particular case $y_{\text{landing}} = 0$ that corresponds to a kink angle $\theta_{\text{tan}} = 90°$. One thus gets $\left[G_{\text{c}}^{\text{inc}}/G_{\text{c}}^{\text{mat}}\right]_{\text{crit}} \sim 3.85$. This value is in close agreement

with the simulation results of Fig. 18 where inclusion by-pass was systematically observed for $G_c^{inc}/G_c^{mat} = 4$, in spite of the different inclusion geometries considered (spherical in Fig. 18, cylindrical here).

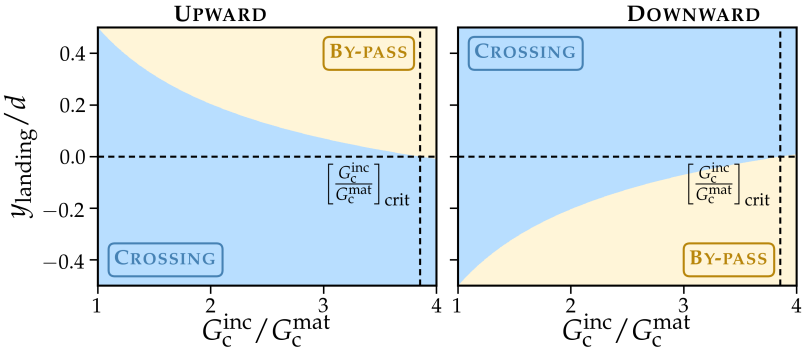

Figure 20: Theoretical phase diagram providing the depinning mechanism (crossing vs by-pass) of a crack pinned by a cylindrical inclusion (see Fig. 19) as a function of the toughness ratio G_c^{inc}/G_c^{mat} and the relative landing height $y_{landing}/d$. Note that the critical toughness ratio $\left[G_c^{inc}/G_c^{mat}\right]_{crit} \sim 3.85$ beyond which the obstacle is systematically by-passed corresponds to the landing height $y_{landing} = 0$ and a kink angle $\theta_{tan} = 90°$.

4.1.2. Comparison of the two-dimensional theoretical model with three-dimensional numerical simulations on spherical inclusions

The transition diagram of Fig. 20 being derived from a simplified two-dimensional theory considering cylindrical inclusions, it is interesting to compare it to the results of fully three-dimensional simulations considering spherical inclusions, as the 3D case is more complex: when depinning (crossing or by-pass) occurs, the local SIFs are already perturbed by the deformations of the crack. The determination of the region of the front that triggers depinning is then not an easy task, and we shall resort to numerical simulations.

The numerical efficiency of our method allows to run several thousands of simulations with GNU Parallel (Tange, 2011), to investigate the impacts of both the toughness ratio between the inclusion and the matrix and the landing height. Since we consider the values $\theta_{ini} = 0$ and $\rho_{II} = 0$, the region $y_{landing}/d \in]-0.5, 0[$ of the phase diagram is deduced by symmetry from the region $y_{landing}/d \in [0, 0.5[$. To draw the diagram, we define the type of depinning mechanism (crossing versus by-pass) from the behavior of the point of the front located in $z = L_z/2$, where θ_{tan} is maximal. Interestingly, the two-dimensional and three-dimensional theoretical diagrams are almost identical, as be seen in Fig. 21. Yet, we shall see in Section 5 that this coincidence breaks down for other shapes of inclusion.

4.2. Impact of the by-pass mechanism on the effective toughness of periodic heterogeneous media

Crack deflection has often been viewed as a toughening mechanism (Faber and Evans, 1983; Suresh, 1985; Steinbrech, 1992), albeit much less efficient than such mechanisms as crack bridging (Bower and Ortiz, 1991). We want here to stress the idea that in the presence of toughness discontinuities, crack deflection must be considered more as a severely limiting factor of material toughening, than as a toughening process *per se*.

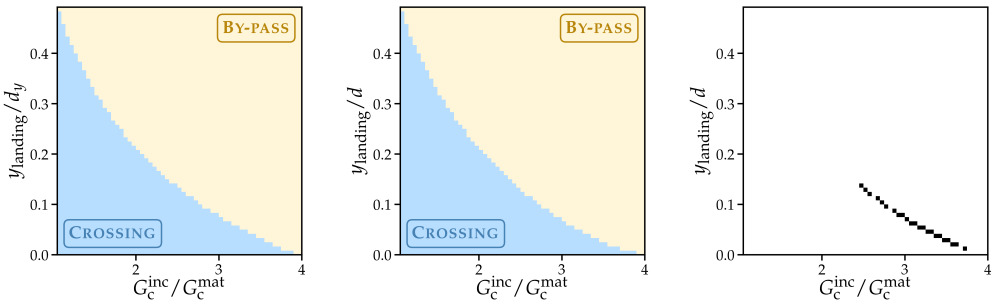

Figure 21: Comparison of two- and three-dimensional transition diagrams: (a) Theoretical two-dimensional diagram for cylindrical inclusions; (b) three-dimensional transition for spherical inclusions obtained from 1200 simulations with various toughness ratios $G_c^{\text{inc}}/G_c^{\text{mat}}$ and landing heights y_{landing}/d; (c) difference between the two diagrams, the black region indicating different behaviors.

4.2.1. Definition of the effective toughness

We first need to define *effective fracture properties*. In agreement with Gao and Rice (1989), Bower and Ortiz (1991), Hossain et al. (2014) and Vasoya et al. (2016a), we define the *effective toughness* as the maximal macroscopic elastic release rate G^∞ (resulting from the variable loading) encountered during *cracking of the whole sample*:

$$G_c^{\text{eff}} = \max_{x\in[0,L_x]} G^\infty(x)\,. \tag{28}$$

This definition is compatible with Griffith's definition of toughness, since if the loading is too low for the value G_c^{eff} to be reached, complete cracking of the specimen cannot occur. An example of the evolution of G^∞, together with the associated definition of G_c^{eff}, are provided in Fig. 22 for the three-dimensional propagation of a crack interacting with a disordered distribution of inclusions with the values $G_c^{\text{inc}} = 1.75\,G_c^{\text{mat}}$ and $G_c^{\text{int}} = G_c^{\text{mat}}$.

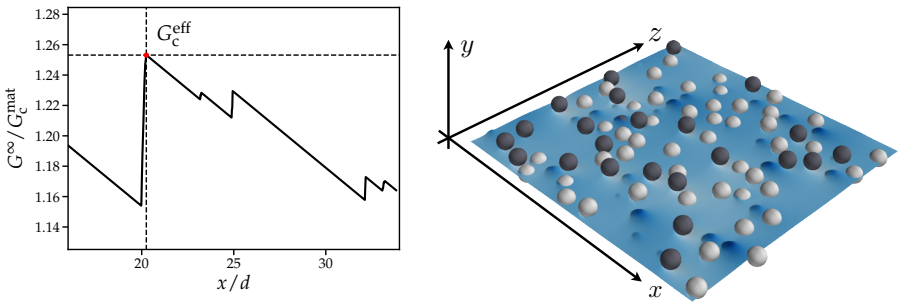

Figure 22: Effective toughness G_c^{eff} defined as the maximum ERR imposed by the variable macroscopic loading G^∞ during cracking of the entire specimen: (a) evolution of G^∞ during crack propagation in the medium-sized disordered system shown in panel (b). The macroscopic ERR G^∞ increases while the front is trapped and decreases when the crack propagates according to Eq. (4).

4.2.2. Inclusion by-pass, a limiting mechanism of toughening through crack front trapping

We consider periodic arrangements of spherical inclusions of diameter $d = L_z/4$. The toughness of the inclusions varies from $G_c^{inc} = G_c^{mat}$ to $4\,G_c^{mat}$ while the interface and the matrix share the same fracture properties, $G_c^{int} = G_c^{mat}$. The crack lands on the inclusions at a height $y_{landing} = 0.1\,d$. The effective toughness is estimated through Eq.(28) from the evolution of the macroscopic ERR G^∞ during crack propagation. Results are plotted in Fig. 23. Convergence of the results with decreasing front mesh size Δz is investigated in Appendix C.

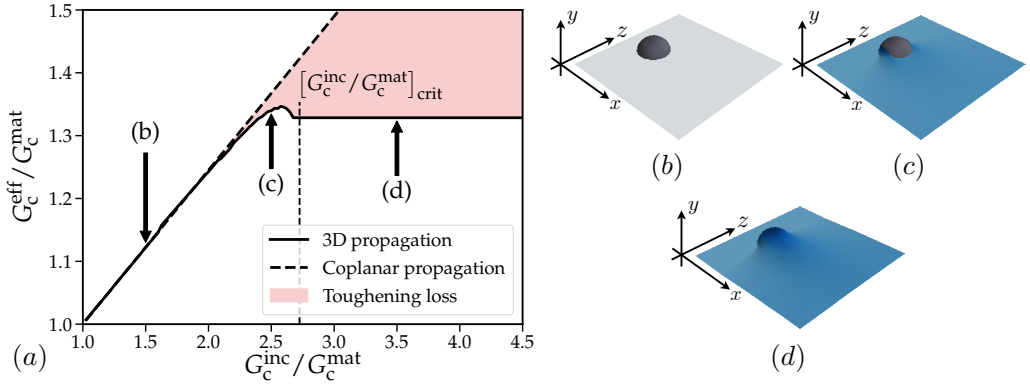

Figure 23: (a) Global impact of the inclusion toughness ratio G_c^{inc}/G_c^{mat} upon the effective toughness G_c^{eff}; (b) crossing regime: the effective toughness increases linearly with the inclusion toughness according to mixture rule of Eq. (30); (c) partial by-pass regime: the region of the crack front close to the center of the inclusion crosses the inclusion, whereas those closer to the edges (where the required deflection angle θ_{tan} is lower) by-pass it; (d) by-pass regime: the effective toughness reaches a plateau. An increase of the inclusion toughness does not toughen the composite any further.

Three regimes may be distinguished here:

1. For low values of the inclusion toughness, up to $G_c^{inc} = 2\,G_c^{mat}$, the effective toughness increases linearly with the inclusion toughness.
2. For medium values of the inclusion toughness, up to $G_c^{inc} = 2.5\,G_c^{mat}$, the "toughening slope" $\frac{\partial G_c^{eff}}{\partial G_c^{inc}}$ gradually decreases and the effective toughness reaches a peak.
3. For high values of the inclusion toughness, above $G_c^{inc} = 2.75\,G_c^{mat}$, the effective toughness reaches a plateau $G_c^{eff} \simeq 1.395\,G_c^{mat}$.

The first regime is characterized by the crossing of the inclusions as depicted in Fig. 23.b. The situation is thus equivalent to the coplanar propagation of a crack encountering a periodic array of circular inclusions. This situation has been investigated by Gao and Rice (1989) and Bower and Ortiz (1991), with the conclusion that a good estimate of the effective toughness is provided by the following expression:

$$\frac{G_c^{eff}}{G_c^{mat}} = 1 + \frac{d}{L_z}\sqrt{1 - 4\left(\frac{y_{landing}}{d}\right)^2}\left[\frac{G_c^{inc}}{G_c^{mat}} - 1\right], \text{ for } G_c^{inc} \leq 2\,G_c^{mat}, \tag{29}$$

where the linearity with respect to the ratio $\dfrac{G_c^{inc}}{G_c^{mat}}$ is apparent. Such prediction is plotted in dashed black line in Fig. 23.

Close but below the critical toughness at the crossing to by-pass transition $\left[G_c^{inc}\right]_{crit} \simeq 2.75\, G_c^{mat}$ for $y_{landing} = 0.1\, d$ (Eq. (27)), we observe a transient regime in which the effective toughness is *larger* than the plateau value corresponding to inclusion by-pass. This implies that the crack crosses the inclusion while by-passing it could have been achieved earlier, at a lower loading level. This rather counter-intuitive observation is discussed in further details in Appendix D. It stems from the *local* propagation criterion that consists in maximizing $G - G_c$ at every location along the front and at every time step. While a *global* optimization would have favored inclusion by-pass. These observations are in line with the experimental findings of Takei et al. (2013), who indeed observed that the choice of crack trajectory corresponds better to a local maximization of $G - G_c$ than some global maximization. This means that the crack propagates following the *locally* weakest path, and can thus globally dissipate more energy than it would by trying to achieve some global minimization, as also discussed in Osovski et al. (2015). This interesting feature definitely needs to be exploited to design tougher materials.

Above the critical toughness $\left[G_c^{inc}\right]_{crit} \sim 2.75\, G_c^{mat}$ (Eq. (27)), the crack interacts with the inclusion through a by-pass mechanism (Fig. 23.d). When the crack by-passes the inclusion, it propagates along the interface so that the inclusion toughness ceases to play any role. This is why a further increase of the inclusion toughness leaves the effective toughness unchanged. The conclusion is that there is a quick (though not instantaneous) shift from a first regime where the inclusion is crossed and the effective toughness of the composite is increased by *crack trapping*, to a second one characterized by the by-pass of the inclusion, which activates a less efficient toughening mechanism, *crack deflection*.

As the landing height $y_{landing}$ increases, the tangent angle θ_{tan} decreases (Eq. (22)), facilitating by-pass that happens for lower values of the inclusion toughness. As a result, the plateau regime is reached earlier, and corresponds to a lower effective toughness, as shown in Fig. 24.a. Predicting G_c^{eff} analytically when crack deflection occurs is difficult. However it is clear that below some critical toughness ratio $\left[G_c^{inc}/G_c^{mat}\right]_{crit}$, the inclusion is crossed and the effective toughness follows Eq. (29), while it reaches a plateau above $\left[G_c^{inc}/G_c^{mat}\right]_{crit}$; using then Eq. (27) in spite of the fact that it strictly applies to 2D situations (cylindrical inclusions), and combining it with (29), one gets the following rough estimate of the effective toughness:

$$\frac{G_c^{eff}}{G_c^{mat}} = 1 + \frac{d}{L_z}\sqrt{1 - 4\left(\frac{y_{landing}}{d}\right)^2}\left[\min\left(\frac{G_c^{inc}}{G_c^{mat}}, \left[\frac{G_c^{inc}}{G_c^{mat}}\right]_{crit}\right) - 1\right] \tag{30}$$

The comparison between the results of numerical simulations and the theoretical predictions of Eq. (30) is plotted in Fig. 24. a & b. One observes that Eq. (30) quantitatively describe the effective toughness in the crossing regime while it only provides an upper-bound prediction during by-pass.

4.2.3. Impact of microstructural parameters on the effective toughness

We now investigate the impact of other microstructural parameters on the effective toughness, namely the inclusion spacing and the interface toughness. The former proves to be a decisive factor for material toughening in the case of coplanar propagation (Gao and Rice, 1989), while the latter is expected to modify the conditions under which inclusion by-pass prevails over its crossing and thus influence the ultimate effective fracture properties of the composite.

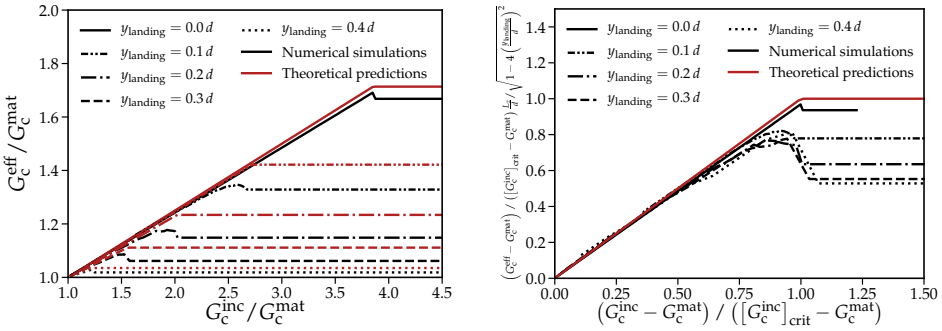

(a) (b)

Figure 24: Impact of the landing height y_{landing} on the effective toughness G_c^{eff} : the crossing/by-pass transition occurs at lower inclusion toughness levels as the landing height increases, making the plateau value decrease accordingly; comparison of numerical simulations (in black) and theoretical predictions of Eq. 30 (in red) for the effective toughness (a); renormalization from Eq. (30) (b).

As the spacing L_z between neighboring inclusions increases, the "toughening slope" $\frac{\partial G_c^{\text{eff}}}{\partial G_c^{\text{inc}}}$ decreases in the linear regime corresponding to crossing of the inclusion (see Fig.25.a). Yet, the critical toughness ratio $\left[G_c^{\text{inc}}/G_c^{\text{mat}}\right]_{\text{crit}}$ does not depend on the inclusion spacing but only on the inclusion mechanical and geometrical properties (see Eq. (27)). Thus the effective toughness reaches a plateau for a well-defined, constant critical toughness ratio $\left[G_c^{\text{inc}}/G_c^{\text{mat}}\right]_{\text{crit}}$, but its height decreases when the inclusion spacing increases as predicted by Eq. (30) (Fig.25.b). The constant value of the critical toughness ratio $\left[G_c^{\text{inc}}/G_c^{\text{mat}}\right]_{\text{crit}}$, irrespective of the value of L_z, is reminiscent of the absence of collective effects in the by-pass of inclusions. In other words, the mechanism selected by the crack during its interaction with an inclusion is not affected by the presence of neighboring inclusions. Note however the lower value of G_c^{eff} in the by-pass regime for the denser arrangement of inclusions ($L_z = 2\,d$). This is signature of collective by-pass of neighboring inclusions, explained by the fact that a lesser portion of the crack drags the front back in the mean fracture plane by long-range elastic effects (see Eq. (6)). Its impact on G_c^{eff} remains nonetheless small when compared to the overall impact of the by-pass mechanism.

Finally, the matrix/inclusion interface may not share the fracture properties of the matrix, namely be weaker $G_c^{\text{int}} < G_c^{\text{mat}}$. Reducing the interface toughness favors inclusion by-pass, which is then triggered at lower inclusion toughness levels (see Fig. 26.a). The impact of a weak interface on the crossing to by-pass transition is well grasped by Eq. (27), as shown by the curve renormalization of Fig. 26.b. Given that the maximum value of the macroscopic loading is reached at the onset of the by-pass event, the effective toughness drops and its plateau value decreases as crack propagation along the weak interface is made easier.

In conclusion, the by-pass mechanism offers a more energetically favorable trajectory for crack propagation. It hinders toughening by limiting crack trapping. In order to toughen brittle materials, one should design inclusion geometries preventing inclusion by-pass; a good example consists of inclusions with a concave interface, for which by-passing becomes more and more difficult as the crack progresses along it. This remark is compatible with the results of topological optimization studies of two-dimensional crack propagation (Da et al., 2018). Concave interfaces emerge from the optimization process, with the consequence of preventing inclusion by-pass and

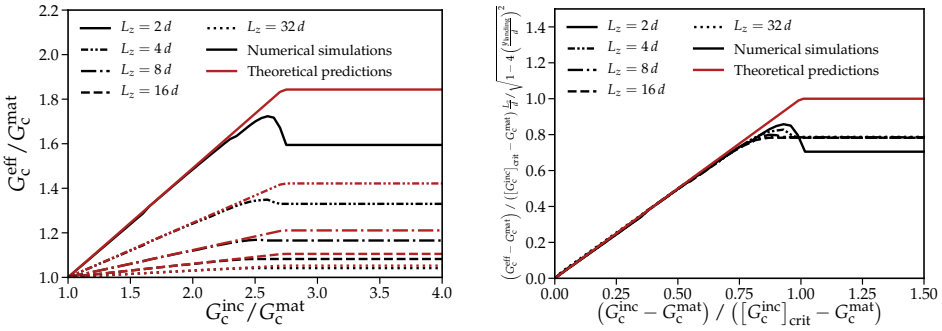

(a) (b)

Figure 25: Impact of the inclusion spacing L_z upon the effective toughness G_c^{eff}: both the slope in the linear regime and the plateau value decrease when the density of tough inclusions decreases; comparison of numerical simulations (in black) and theoretical predictions of Eq. (30) (in red) for the effective toughness (a) ; renormalization of the curves of panel (b) using the expression (30) of the effective toughness and a constant value $\left[G_c^{\mathrm{inc}}/G_c^{\mathrm{mat}}\right]_{\mathrm{crit}} = 2.75$ of the toughness ratio at the crossing/by-pass transition.

promoting crack nucleation on the other side of the inclusion. This phenomenon ultimately leads to crack bridging, which has been identified as a particularly efficient toughening mechanism (Bower and Ortiz, 1991).

5. Inclusion shape as a limiting factor of material toughening

All previous results have been obtained for spherical inclusions. For such an inclusion shape, the interaction mechanisms are fairly well predicted by a simple two-dimensional theoretical analysis considering cylindrical inclusions, the explanation being that the difference between the macroscopic and local SIFs is small. We now investigate the case of spheroidal inclusions elongated along the crack front direction, and bring out a new effect: the coupling of the in-plane and out-of-plane deformations of the front may modify the conditions of occurrence of the crossing/by-pass transition, with a dramatic impact on the effective toughness of three-dimensional heterogeneous materials.

5.1. Collective by-pass of prolate spheroidal inclusions

We consider prolate spheroidal inclusions elongated in the direction z of the crack front. The length of the i-th principal axis is denoted d_i. We consider two inclusion geometries, the first with $d_z = d$, $d_x = d_y = d/2$, and the second with $d_z = d$, $d_x = d_y = d/4$, as shown in Fig. 27. For both geometries, the crossing/by-pass transition diagram is obtained by the same procedure as for spherical inclusions, see Section 4.1. Results are plotted in Fig. 28 and 29.

One immediately notes that the new diagrams fundamentally differ from that obtained for spherical inclusions, Fig. 21. For prolate spheroidal inclusions elongated in the z-direction, the by-pass mechanism happens at lower inclusion toughness levels than for the cylindrical (2D) and spherical geometries. This is a consequence of the coupling of the in-plane and out-of-plane deformation modes of the crack front, which is enhanced by the new inclusion geometry, as will now be detailed.

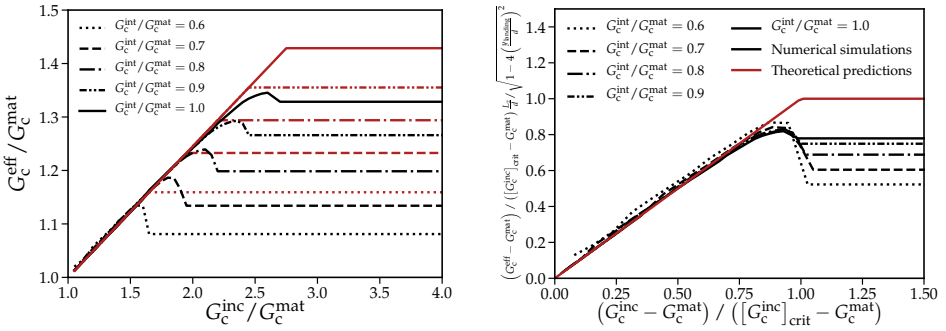

(a) (b)

Figure 26: Impact of the interface toughness G_c^{int} upon the effective toughness G_c^{eff}: the crossing/by-pass transition occurs at lower inclusion toughness levels as the interface toughness decreases and by-passing is facilitated by the weaker interface making the plateau value decrease; comparison of numerical simulations (in black) and theoretical predictions of Eq. (30) (in red) for the effective toughness (a) ; renormalization of the curves of panel (b) using the expression (30) of the effective toughness and a varying value $\left[G_c^{inc}\right]_{crit} = 2.75\, G_c^{int}$ of the toughness ratio at the crossing/by-pass transition.

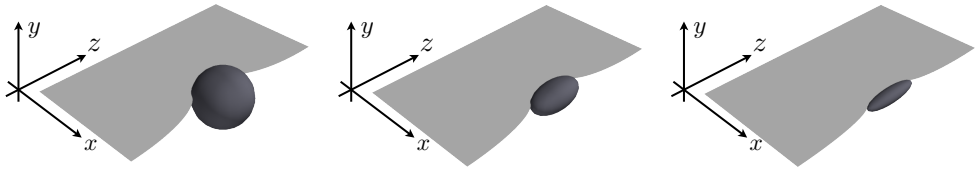

(a) (b) (c)

Figure 27: Interaction of a crack with spheroidal inclusions elongated in the direction of the crack front: the inclusion is either spherical (a) or prolate spheroidal, with axes $d_z = d_x = 2\, d_y$ (b) or $d_z = 4\, d_x = 4\, d_y$ (c).

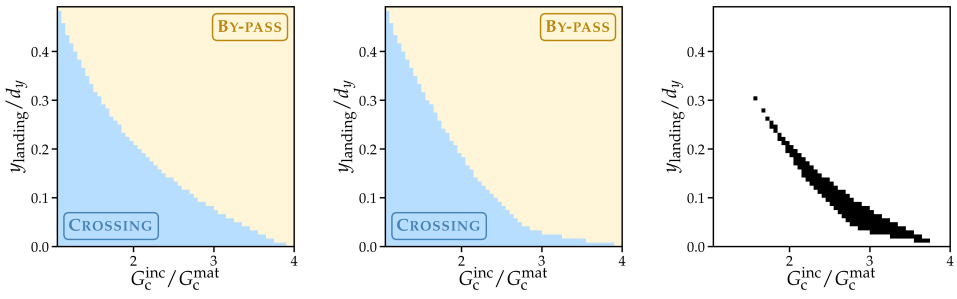

(a) (b) (c)

Figure 28: Comparison of two- and three-dimensional transition diagrams for prolate spheroidal inclusions with $d_z = 2\, d_x$: (a) Two-dimensional diagram for cylindrical inclusions; (b) three-dimensional transition diagram for spheroidal inclusions obtained from 1200 simulations with various toughness ratios G_c^{inc}/G_c^{mat} and landing heights $y_{landing}/d$; (c) difference between the two diagrams - the black regions indicate different behaviors.

In the case of prolate spheroidal inclusions elongated in the direction z of the crack front, pinning of the front stops earlier near the edges of the inclusion than in its central region. This is

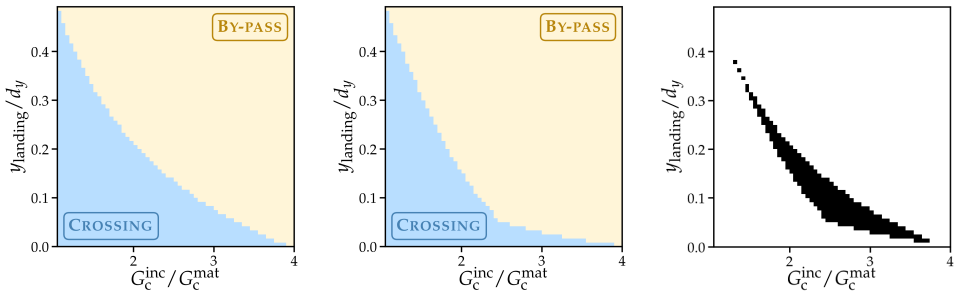

(a) (b) (c)

Figure 29: Comparison of two- and three-dimensional transition diagrams for prolate spheroidal inclusions with $d_z = 4\,d_x$: (a) Two-dimensional diagram for cylindrical inclusions; (b) three-dimensional transition diagram for spheroidal inclusions obtained from 1200 simulations with various toughness ratios $G_c^{\text{inc}}/G_c^{\text{mat}}$ and landing heights y_{landing}/d; (c) difference between the two diagrams - the black regions indicate different behaviors.

due to the fact that the long-range elastic interaction term of the perturbed SIFs is sensitive to the local crack front curvature, as underlined in Eq. (19). In Fig. 30, we plot the perturbation of the Mode I SIF along the crack front, when pinned by the three geometrically different inclusions considered. In the spherical case, the perturbation of the SIF is maximal at the center of the crack front (see Fig. 30.d); therefore unpinning occurs there first. For prolate spheroidal inclusions, the perturbation of the SIF is lower in the central part of the crack front, due to a larger in-plane curvature (Fig. 30.b & 30.e); therefore unpinning occurs near the edges of the inclusion first.

This difference in depinning dynamics has a decisive impact on out-of-plane deviations of the crack. The points located near the edges of the inclusion "see" a lower tangent angle θ_{tan} and thus are more prone to by-passing the inclusion. Therefore, when the central point unpins, the out-of-plane configuration of the crack front is very different for spherical and prolate spheroidal inclusions. This out-of-plane configuration is plotted in Fig. 31(a-c) for the three geometries considered here. For the spherical inclusion, the front is almost flat when the central point begins to by-pass the inclusion; the central point is loaded in pure Mode I and thus follows the theoretical two-dimensional predictions of Eq. (27). For the prolate spheroidal inclusions, the points of the crack front located near the edges of the inclusion have already begun to by-pass it when the central point unpins. The out-of-plane deformation of the front generates a negative long-range Mode II perturbation δK_{II} at these points, see Fig. 31(d-f). At the central point, G is no longer maximal in the direction $\theta = 0°$ but in the direction $\theta_{\text{max}} \simeq -2\delta K_{\text{II}}/K_{\text{I}}^{\infty} > 0$, thus favoring an upward by-pass of the inclusion.

Three-dimensional effects arising from a non-spherical inclusion geometry can thus drastically lower the inclusion toughness level at which the crossing/by-pass transition occurs. These effects are inherently collective since they are caused by long-range elastic interactions along the crack front, occurring both within the unperturbed crack plane (with consequences upon propagation dynamics) and out of this plane (with consequences upon the crack trajectory).

Note that this collective behavior is observed in the quasi-static limit $v_m \ll v_0$. Increasing the driving velocity may change the pinning dynamics and suppress collective crack motion. Namely, when $v_m \simeq v_0$, the central region of the crack front unpins immediately after landing on the inclusion when the crack front is still flat $f_y = 0$, preventing collective effects from occurring. At such driving velocities, the crossing/by-pass transition follows the predictions of Eq. (27).

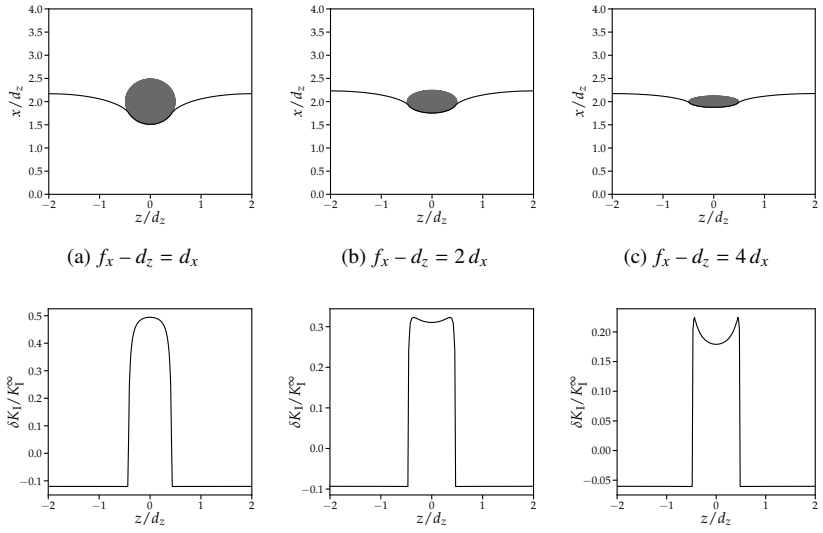

(a) $f_x - d_z = d_x$ (b) $f_x - d_z = 2\,d_x$ (c) $f_x - d_z = 4\,d_x$

(d) $\delta K_I - d_z = d_x$ (e) $\delta K_I - d_z = 4\,d_x$ (f) $\delta K_I - d_z = 2\,d_x$

Figure 30: Impact of the in-plane perturbation of the crack front on crack depinning dynamics: the in-plane perturbation f_x is plotted just before depinning of the central point of the front, for a spherical inclusion (a), and two different prolate spheroidal inclusions (b) and (c). The associated perturbations of the Mode I SIF δK_I are plotted in (d-f); unpinning occurs first at the central point of the front for a spherical inclusion, but near the edges of the obstacle for prolate spheroidal inclusions.

5.2. Impact of collective, three-dimensional effects upon the effective toughness

The change in the conditions governing the crossing/by-pass transition is expected to have a subsequent impact upon the effective toughness of materials containing periodic arrangements of tougher inclusions. To address this issue, we consider a crack interacting with the three types of tough inclusions considered above; the system size is $L_z = 4\,d = 4\,d_z$. We fix the geometrical ratio $L_z/d_z = 4$ in order to fix the effective toughness corresponding to inclusion crossing, and the landing height $y_\mathrm{landing} = 0.1\,d_y$ so that the central point of the crack front (where the kink angle is maximum) always "sees" the same tangent angle θ_tan; but we vary the ratio $G_\mathrm{c}^\mathrm{inc}/G_\mathrm{c}^\mathrm{mat}$ of the inclusion and matrix toughnesses. The results are plotted in Fig. 32.

In the case of prolate spheroidal inclusions, the lower toughness threshold for the crossing/by-pass transition induces a dramatic loss of toughening, as expected from the previous analysis of the crack trajectory. The value of the critical toughness ratio above which the inclusion is systematically by-passed is, for $y_\mathrm{landing}/d = 0.1$, $\left[G_\mathrm{c}^\mathrm{inc}/G_\mathrm{c}^\mathrm{mat}\right]_\mathrm{crit} \simeq 2.25$ for $d_z = 2\,d_x$, and $\left[G_\mathrm{c}^\mathrm{inc}/G_\mathrm{c}^\mathrm{mat}\right]_\mathrm{crit} \simeq 2.05$ for $d_z = 4\,d_x$, to be compared to the two-dimensional theoretical value $\left[G_\mathrm{c}^\mathrm{inc}/G_\mathrm{c}^\mathrm{mat}\right]_\mathrm{crit} \simeq 2.75$ for a spherical inclusion. Quite logically, this lower critical toughness ratio has a strong impact upon the plateau value of the effective toughness. Whereas the effective toughness reaches the plateau value $G_\mathrm{c}^\mathrm{eff} \simeq 1.328\,G_\mathrm{c}^\mathrm{mat}$ in the spherical case, this value falls down to $G_\mathrm{c}^\mathrm{eff} \simeq 1.267\,G_\mathrm{c}^\mathrm{mat}$ for $d_z = 2\,d_x$, and even $G_\mathrm{c}^\mathrm{eff} \simeq 1.160\,G_\mathrm{c}^\mathrm{mat}$ for $d_z = 4\,d_x$.

The toughening reduction results from the three-dimensional coupling of the in-plane and out-of-plane deformation modes of the crack front, which modifies the interactions of the crack

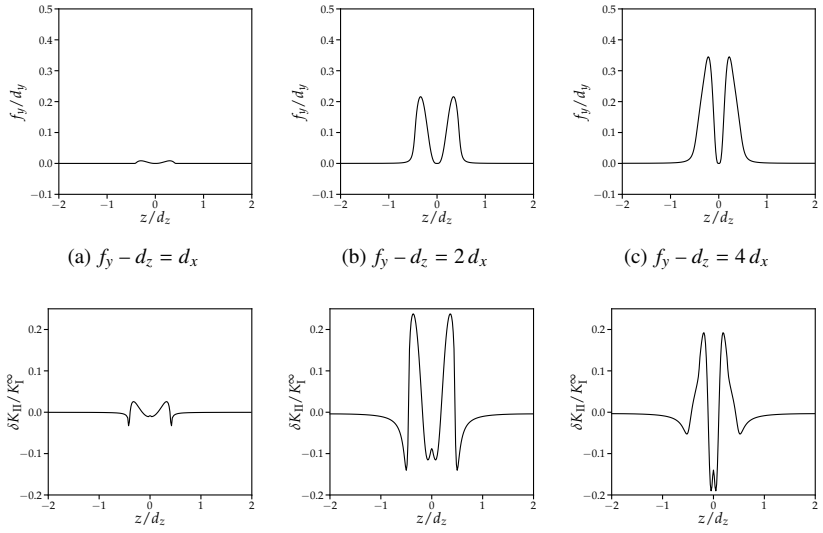

(a) $f_y - d_z = d_x$ (b) $f_y - d_z = 2\,d_x$ (c) $f_y - d_z = 4\,d_x$

(d) $\delta K_{II} - d_z = d_x$ (e) $\delta K_{II} - d_z = 2\,d_x$ (f) $\delta K_{II} - d_z = 4\,d_x$

Figure 31: Impact of the out-of-plane perturbation of the crack front on crack trajectory: The out-of-plane perturbation f_y is plotted just before the depinning of the central point of the front, for a spherical inclusion (a), and two different prolate spheroidal inclusions (b) and (c). The associated perturbations of the Mode II SIF δK_{II} are plotted in (d-f); in the spheroidal case, the non-zero value of δK_{II} at the central point of the front means that those points of the front located near the edges of the inclusion exert a pulling force on it perpendicularly to the mean crack plane.

and the inclusions, and consequently the effective toughness of the composite. This coupling was disregarded in previous three-dimensional perturbative studies (Ramanathan et al., 1997; Barès et al., 2014), where only the question of crack trajectory was addressed; yet what precedes unambiguously shows that it must be accounted for in studies of effective fracture properties of three-dimensional heterogeneous materials.

6. The by-pass mechanism as a limiting factor of both crack trapping and crack bridging

We have just showed how the by-pass mechanism may induce a substantial toughening loss, by limiting material toughening through crack trapping. But crack trapping can only increase the effective toughness by a factor two or three. Crack bridging is mentioned in the literature as a much more interesting toughening mechanism, since it may increase the material toughness by a factor of 10 to 60, as experimentally observed by Krstic et al. (1981) and confirmed numerically by Bower and Ortiz (1991). When long fibers remain unbroken in the wake of the crack, they hinder the opening of the crack behind the front, so that a greater load is required to induce propagation. Such features have been observed in nature, in biological materials such as bone and nacre, displaying remarkable toughness properties (Barthelat et al., 2007; Wegst et al., 2015). These observations have triggered the development of bio-inspired materials, in which toughness properties are adjusted so as to favour crack bridging (Mirkhalaf et al., 2014; Wegst et al., 2015). Yet, whereas crack deflection permits crack bridging to happen in the case of fibers (Evans et al., 1991; Naslain, 1998), it is shown in this section that such is not systematically the case for any inclusion shape, because inclusion by-pass may hinder crack bridging.

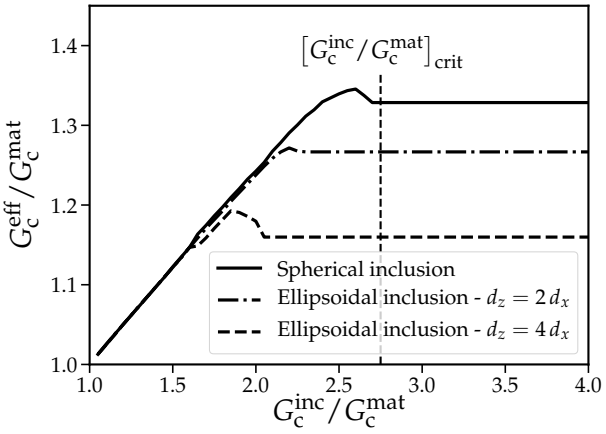

Figure 32: Impact of the aspect ratio of the inclusions upon the effective toughness G_c^{eff} : prolate spheroidal inclusions elongated in the direction of the crack front are by-passed by the crack at lower toughness levels because of three-dimensional collective effects, resulting in a lowering of the plateau value of the effective toughness.

Bower and Ortiz (1991) showed that if the inclusions are tough enough, the crack front bows around the inclusion within its plane, and the parts of this front passing the inclusion on its left and right coalesce behind it, leaving it in the wake of the crack front. They emphasized that crack bridging already occurs for inclusions 4.4 times tougher than the matrix, i.e. for $G_c^{inc}/G_c^{mat} \geq 4.4$. However, we showed in Section 4 that by-pass systematically happens for spherical inclusions with toughness ratios $G_c^{inc}/G_c^{mat} \geq 3.82$, implying that bridging *cannot* occur for spherical inclusions since by-pass prevails over crack front trapping. Thus, as crack bridging *does* happen for infinitely elongated fibers along the y-direction, one may wonder how elongated should an inclusion be for crack bridging to prevail over inclusion by-pass.

To address this issue, we consider the interaction of a semi-infinite crack with periodic arrangements of prolate spheroidal inclusions elongated in the y-direction, having $d_z = d_x = d$ and$0.1 \leq d_y/d \leq 4$ (see Fig. 33). We consider a toughness ratio $G_c^{inc} = 4\,G_c^{mat}$, that corresponds to the upper limit of the validity range of our model (see Section 2.4). We do not model crack bridging, but rather focus on the estimation of the conditions under which this mechanism may occur or not. We compare our results, based on the modeling of the coupling of crack trapping and inclusion by-pass, to those obtained for the coupling of crack trapping and bridging by Bower and Ortiz (1991).

For the toughness contrast and aspect ratios of inclusion considered, the by-pass mechanism prevails over inclusion crossing. We then compute the loading required to by-pass the inclusion - that is the effective toughness of the composite - and compare it to that for which crack bridging is expected to occur. The latter, determined by Bower and Ortiz (1991), corresponds to the loading required to ensure crack coalescence around a cylindrical inclusions of axis perpendicular to the crack plane. It depends only on the ratio of the inclusion effective radius (that varies with the landing height) over the particle inter-distance L_z. The procedure, repeated for various landing height $y_{landing}/d_y$, leads to the results of Fig. 34.

For a given landing height $y_{landing}$, the effective toughness increases with the aspect ratio d_y/d_z. This is due to the fact that the crack front is dragged downward because of the growing

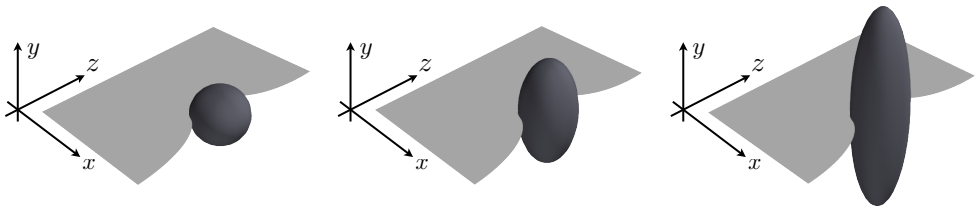

(a) (b) (c)

Figure 33: Inclusion geometries considered in the study of the by-pass/bridging transition: spherical (a), prolate spheroidal with $d_y = 2\,d_z = 2\,d_x$ (b) or $d_y = 4\,d_z = 4\,d_x$ (c)

Mode II contribution δK_{II} while it is by-passing the inclusion upwards. The more elongated the inclusion, the harder the by-passing - and therefore the larger the load required to induce crack propagation - because of the larger difference between the propagation direction θ_{tan} and that, θ_{max}, corresponding to the maximum of G. We see that even for elongated inclusions, typically $d_y/d = 4$, crack bridging is not activated before by-pass can be fully completed.

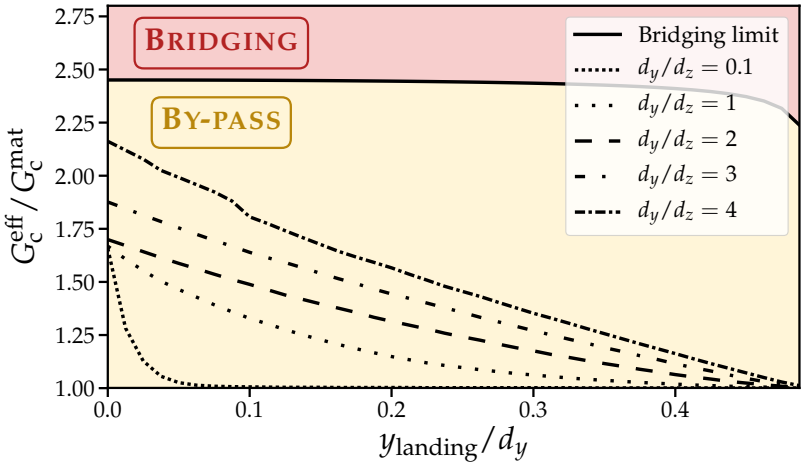

Figure 34: By-pass/bridging transition as a function of the normalized landing height y_{landing}/d_y for different inclusion aspect ratios d_y/d_z: the effective toughness corresponding to the by-pass mechanism (in dashed/dotted line) is compared to the predicted effective toughness at the crack trapping/bridging transition (in solid line).

We conclude that in the limit of very long fibers ($d_y/d_z \to +\infty$), Bower and Ortiz (1991)'s numerical predictions of toughening through crack bridging applies. Yet, as soon as obstacles of finite elongation are considered, inclusion by-pass prevents crack bridging, thus considerably reducing the material toughening due to inclusions. However these conclusions remain qualitative insofar as, strictly speaking, our first-order model remains rigorously valid for small out-of-plane deviations, a condition which is violated as soon as the inclusion gets too much elongated. Moreover, Xu et al. (1998) showed that crack branching may occur at the matrix/inclusion interface. This type of branching is not included in our model which considers only a single macroscopic crack. It may induce an increase of the energy dissipated by crack propagation and thus delay

inclusion by-pass, allowing the trapping/bridging transition to occur.

7. Limitations of the proposed approach

In this paper, we propose a new LEFM-based theoretical framework allowing to model crack propagation in large-scale three-dimensional heterogeneous brittle materials. If this framework is applied here to investigate the mechanisms of interaction between a crack and tough inclusions in a periodic setting, it has been developed to model crack propagation in large-scale disordered composites containing millions of tough inclusions (see Fig. 15). Reaching such unprecedented numerical performances requires to make strong assumptions that consequently limit the scope of the proposed approach. In particular, (i) only toughness inclusions possessing the same elastic properties as the matrix material are considered and (iii) micro-cracking ahead of the main crack as well as (ii) crack branching are ignored. These mechanisms and their relative impact are discussed below.

First, we assume that *the matrix and the inclusions share the same elastic properties* and only differ in their fracture properties. Yet elastic heterogeneities have been shown in the literature to impact both the crack trajectory and the effective fracture properties. In particular, (i) elastic inclusions have volume attracting/repelling effects on crack propagation (Gao, 1991; Bush, 1997; Clayton and Knap, 2014; Lacondemine et al., 2017), while (ii) discontinuities of elastic properties at the matrix/inclusion interface does not only trigger crack deflection (He and Hutchinson, 1989) but also crack trapping through denucleation/renucleation processes (Leguillon and Martin, 2013). All those effects have been shown to impact the effective toughness of composite materials (Li and Zhou, 2013; Hossain et al., 2014; Brach et al., 2019).

The perturbative approach developed in this paper, which allows to estimate SIF variations arising from geometrical perturbations of the crack front, could be coupled at first-order to the formulæ of Gao (1991) extended by Muju (2000), which provide SIF perturbations induced by mild variations of the elastic properties. Such an extension would provide quantitative results on the influence of volume effects triggered by moderate spatial variations of Young's Modulus E or Poisson's ratio ν on the effective fracture properties of heterogeneous solids. Yet, the local SIF estimation will then require to compute volume integrals over the whole domain and come at a higher computational cost, making large-scale simulations impossible to achieve.

Moreover, such an approach will be restricted to smooth variations of elastic properties since, to the best of the authors' knowledge, no analytical framework provides the quantitative tools to handle crack deflection and denucleation/renucleation processes at an elastic interface *in three-dimensions*.

Second, the proposed approach models the growth of a single crack, *ignoring micro-cracking ahead of the crack tip*. Micro-cracking has been shown in the literature to strongly impact effective fracture properties through the competition of weakening by micro-crack coalescence and toughening by micro-crack shielding (Evans and Faber, 1981; Ortiz, 1987, 1988). Note that failure is here purely brittle and micro-cracking processes mentionned in Ortiz (1987) and Ortiz (1988) are confined within the process zone, whose size ℓ_{FPZ} is negligible when compared to the size d of the inclusion. Their impact is thus encompassed in the value of the fracture energy G_{c} of the materials. Moreover, no micro-cracking induced by inclusion debonding (Evans and Faber, 1981) can take place when the scale separation condition $\ell_{\text{FPZ}} \ll d$ is fulfilled. Indeed, let

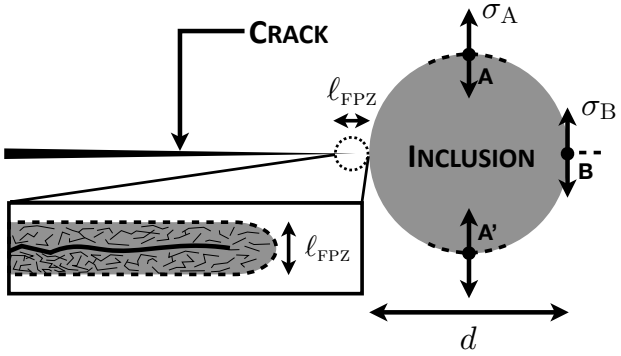

Figure 35: Crack landing on an inclusion, potentially leading to inclusion debonding along the interface (Point A & A') or ahead of the inclusion (Point B).

us consider that all materials (matrix, inclusion, interface) share the same process zone size ℓ_{FPZ}. It relates to the material toughness K_{Ic} and its strength σ_c through (Barenblatt, 1962):

$$\ell_{FPZ} = \frac{\pi}{8}\left(\frac{K_{Ic}}{\sigma_c}\right)^2 \tag{31}$$

Considering that debonding may occur either at the top the inclusion along the interface (Point A and A' in Fig. 35) or ahead of the inclusion (Point B in Fig. 35), we compute the opening stress σ on these points and compare it to the material strength σ_c:

$$\sigma_A = \frac{2}{\pi} 2^{1/4} \frac{K_{Ic}^{inc}}{K_{Ic}^{int}} \sqrt{\frac{\ell_{FPZ}}{d}} \sigma_c^{int} \text{ and } \sigma_B = \frac{2}{\pi} \frac{K_{Ic}^{inc}}{K_{Ic}^{mat}} \sqrt{\frac{\ell_{FPZ}}{d}} \sigma_c^{mat} \tag{32}$$

The scale separation condition $\ell_{FPZ} \ll d$ of Eq. (1) thus implies that no micro-cracking through inclusion debonding can take place, as long as we consider only mild variations of toughness K_{Ic} i.e. G_c. The study presented here provide thus quantitative predictions on the effective toughness in the brittle limit $\ell_{FPZ} \ll d$. Advanced numerical methods such as phase-field models may allow to study the influence of micro-cracking beyond this limit (Nguyen et al., 2016, 2017a).

Third, the pertubative approach only provides explicit formulæ of the local SIF variations for limited reference crack geometries. Thus, *it does not provide an appropriate framework to investigate the influence of crack branching* on the effective toughness. Crack branching may occur at the matrix/inclusion interface if the crack is pinned long enough on the inclusion Xu et al. (1998). Additional energy is then dissipated to make both crack grow further and the effective toughness of the composite is expected to increase. Yet, as suggested by phase-field simulations conducted by Brach et al. (2019), crack branching may not take place in the brittle limit $\ell_{FPZ} \ll d$ as long as the crack lands on an inclined interface and the toughness contrast is moderate. Our study provides thus quantitative results on the effective toughness except when the toughness of the interface is significantly lower than the one of the matrix or when the crack lands on the equatorial plane of the inclusion, facing thus a 90° interface.

Conclusion

This study analyzes the interaction mechanisms between a crack and a tough inclusion in a fully three-dimensional setting, allowing for out-of-plane excursions of the crack front around obstacles. A LEFM-based perturbative framework, accounting for the toughness discontinuity at the matrix/inclusion interface, has been developed in order to predict the spatio-temporal evolution of the front as it deforms and finally escapes from tough inclusions. Our model captures the complex coupling between in-plane and out-of-plane deformation modes of the front during its interaction with the inclusion, while remaining computationally very efficient. It is used to explore the ability of tough inclusions to efficiently trap a crack, and compute the effective fracture resistance of brittle composites reinforced by periodic arrangements of these inclusions. The conclusions drawn from our study are the following:

- Crack path selection and the resulting fracture properties emerge from a competition between two depinning mechanisms, namely inclusion crossing, wherein the crack propagates through the obstacle, and inclusion by-pass, wherein instead the crack front gets around it.

- The selection of one mechanism with respect to the other can be rationalized using the generalized maximum energy release rate criterion that compares the drop in elastic energy release rate due to crack kinking during by-pass with the gain in fracture energy resulting from cracking the matrix instead of the inclusion. It depends on the landing height of the crack on the obstacle that sets the kink angle required for by-passing, the toughness of the inclusion and that of the interface. A simplified two-dimensional theory developed for cylindrical inclusions with axis parallel to the crack front accounts for the transition from crossing to by-pass observed in fully three-dimensional numerical simulations of cracks interacting with spherical inclusions.

- This theory also accounts for the existence of a critical inclusion toughness $G_c^{\text{inc}} \simeq 3.85\, G_c^{\text{mat}}$ above which spherical inclusion are systematically by-passed.

- The by-pass of inclusions has a dramatic impact on the effective fracture properties of the material. It limits inclusion-induced toughening through crack front trapping, by allowing the crack to follow a more energetically favored path. As a result, the effective toughness of the composite does not increase monotonically with the toughness inclusion, but instead reaches a plateau value that cannot be overcome by increasing further the inclusion resistance.

- The toughening of periodic composites can be limited even further by the inclusion shape. The three-dimensional coupling of the in-plane and out-of-plane deformation modes of the crack front can trigger collective effects which facilitate the by-pass of tough prolate spheroidal inclusions elongated in the direction of the crack front. In this case, crack deflection prevails over crack trapping even for rather low values of the inclusion toughness, thus further limiting the reinforcement of brittle material by tough inclusions. This means that the obstacle geometry plays a decisive role on the effective toughness of heterogeneous brittle materials. This conclusion paves the way to more ambitious inclusion design strategies, for example through additive manufacturing techniques.

- Out-of-plane excursions of the crack not only limit material reinforcement through crack front trapping, but may also hinder other efficient toughening mechanisms such as crack bridging. Bower and Ortiz (1991) showed that crack bridging occurs for inclusions at least 4.4 times tougher than the matrix. This lower limit being larger than the critical toughness for by-pass of *spherical* inclusions, crack bridging cannot occur for such inclusions. Considering then *prolate spheroidal* inclusions elongated in the direction perpendicular to the fracture plane, we show that crack deflection triggered by inclusion by-pass prevails over crack bridging for inclusion aspect ratios $d_y/d_z \lesssim 4$. However these predictions might be of qualitative value only, since our model disregards possible crack branching at the matrix/inclusion interface (Xu et al., 1998).

Our study shows that the selection of the depinning mechanism (crossing or by-pass) determines the nature of the toughening mechanism (crack front trapping, crack deflection or crack bridging), and ultimately the overall toughness of the composite material. The complete resolution of the spatio-temporal evolution of the crack front during its interaction with tough inclusions is then necessary to address the issue of the effective fracture properties of reinforced brittle solids. The study focused on rather simple systems (periodic media with only one tough inclusion per period), but our LEFM-based perturbative model displays unprecedented numerical performances, which permit to simulate crack propagation in large-scale heterogeneous materials - something currently out-of-reach of standard numerical approaches like the finite element method. The issue of the effective fracture properties of media containing complex, disordered distributions of tough inclusions will be the topic of a future paper (Lebihain et al., 2020). The in-depth understanding of the interaction mechanisms developed in this paper for simple systems will be essential for the estimation of homogenized fracture properties of more complex ones.

Appendix A Large-angle regularization

In our simulations, the local slope of the crack front in the (xOy) plane, $\partial f_y/\partial x$, may be large during the by-passing of inclusions. To deal with this issue, we propose heuristic, approximate expressions of the SIFs and related quantities based on a combination of Eqs. (6) (Movchan et al., 1998) and (9) (Leblond, 1999).

A.1 Expressions of the stress intensity factors

We consider a point P of abscissa z along the crack front $\mathcal{F}$, and note $\theta = \arctan\left(\partial f_y/\partial x\right)$ the angle (which may be arbitrary large) between with the x-direction and the local direction of crack propagation. Movchan et al. (1998)'s formulæ provide the variations of the SIFs arising from infinitesimal perturbations of the crack front and crack surfaces, to first order in these perturbations, that is for small values of θ. One observes in Eq. (6) that the Mode II variation can be split into a local term $\delta K_{\mathrm{II}}^{\mathrm{loc}}$ proportional to the slope $\partial f_y/\partial x$, and a term $\delta K_{\mathrm{II}}^{\mathrm{LR}}$ depicting long-range elastic interactions:

$$\delta K_{\mathrm{II}}(z,t) = \underbrace{\frac{K_{\mathrm{I}}^{\infty}(t)}{2}\frac{\partial f_y}{\partial x}(z,t)}_{\delta K_{\mathrm{II}}^{\mathrm{loc}}} + \underbrace{\frac{2-3\nu}{2-\nu}\frac{K_{\mathrm{I}}^{\infty}(t)}{2\pi}\,\mathrm{PV}\int_{-\infty}^{+\infty}\frac{f_y(z,t)-f_y(z',t)}{(z-z')^2}\,dz'}_{\delta K_{\mathrm{II}}^{\mathrm{LR}}} \tag{33}$$

(Note that the expressions for the Mode I and III variations do not, however, contain any similar term proportional to $\partial f_y/\partial x$).

On the other hand Leblond (1999)'s formulæ relate the values of the SIFs after an abrupt change of the direction of propagation to those of the SIFs before this change, for an extension of vanishingly small length but an arbitrary kink angle.

We therefore propose, for a crack slightly perturbed out of its plane but with a possibly large slope $\partial f_y/\partial x$, to adopt the following formulæ combining Eqs. (6) and (9):

$$\begin{cases} K_{\mathrm{I}}(z,t) = F_{\mathrm{I,I}}(\theta)\left[K_{\mathrm{I}}^{\infty}(t) + \delta K_{\mathrm{I}}(z,t)\right] + F_{\mathrm{I,II}}(\theta)\,\delta K_{\mathrm{II}}^{\mathrm{LR}}(z,t) \\ K_{\mathrm{II}}(z,t) = F_{\mathrm{II,I}}(\theta)\left[K_{\mathrm{I}}^{\infty}(t) + \delta K_{\mathrm{I}}(z,t)\right] + F_{\mathrm{II,II}}(\theta)\,\delta K_{\mathrm{II}}^{\mathrm{LR}}(z,t) \\ K_{\mathrm{III}}(z,t) = F_{\mathrm{III,III}}(\theta)\,\delta K_{\mathrm{III}}(z,t) \end{cases} \tag{34}$$

Note that:

- For *small angles* θ, Eq. (34) reduces to Eq. (6), as desired, by virtue of the following low-order expressions of the functions $F_{\mathrm{i,j}}(\theta)$ (Leblond, 1999):

$$\begin{cases} \theta = \arctan\left(\dfrac{\partial f_y}{\partial x}\right) = \dfrac{\partial f_y}{\partial x} + O\left[\left(\dfrac{\partial f_y}{\partial x}\right)^3\right] \\ F_{\mathrm{I,I}}(\theta) = 1 + O\left(\theta^2\right) \\ F_{\mathrm{I,II}}(\theta) = -\frac{3}{2}\theta + O\left(\theta^3\right) \\ F_{\mathrm{II,I}}(\theta) = \frac{1}{2}\theta + O\left(\theta^3\right) \\ F_{\mathrm{II,II}}(\theta) = 1 + O\left(\theta^2\right) \end{cases} \tag{35}$$

- If the crack lands on an inclusion with a zero angle and subsequently kinks along the interface, at the *very beginning of the by-pass* Eq. (34) reduces to (9) and is therefore rigorously correct even for large values of the kink angle.

A.2 Expression of the energy-release-rate

Let us consider, as before, a point P on the perturbed crack front $\mathcal{F}$. The local direction of crack propagation makes an arbitrary angle θ with the x-direction. The elastic ERR rate for a kink angle α is given by:

$$G(\alpha) = \frac{1-\nu^2}{E}\left(K_{\mathrm{I}}^2(\alpha) + K_{\mathrm{II}}^2(\alpha)\right) + \frac{1+\nu}{E}K_{\mathrm{III}}^2(\alpha) \tag{36}$$

where $K_{\mathrm{I}}(\alpha)$, $K_{\mathrm{II}}(\alpha)$ and $K_{\mathrm{III}}(\alpha)$ are given by Leblond (1999)'s formulæ :

$$\begin{cases} K_{\mathrm{I}}(\alpha) = F_{\mathrm{I,I}}(\alpha)\,K_{\mathrm{I}}(z,t) + F_{\mathrm{I,II}}(\alpha)\,K_{\mathrm{II}}(z,t) \\ K_{\mathrm{II}}(\alpha) = F_{\mathrm{II,I}}(\alpha)\,K_{\mathrm{I}}(z,t) + F_{\mathrm{II,II}}(\alpha)\,K_{\mathrm{II}}(z,t) \\ K_{\mathrm{III}}(\alpha) = F_{\mathrm{III,III}}(\alpha)\,K_{\mathrm{III}}(z,t) \end{cases} \tag{37}$$

where the SIFs ($K_i(z,t)$) are given by Eq. (34).

Discarding second-order terms in the crack perturbation, we get :

$$G\left(\alpha,\theta,\frac{\delta K_{\mathrm{I}}}{K_{\mathrm{I}}^{\infty}},\frac{\delta K_{\mathrm{II}}^{\mathrm{LR}}}{K_{\mathrm{I}}^{\infty}}\right)=G^{\infty}\left[g_{\mathrm{I}}(\alpha,\theta)\left(1+2\frac{\delta K_{\mathrm{I}}}{K_{\mathrm{I}}^{\infty}}\right)+g_{\mathrm{II}}(\alpha,\theta)\frac{\delta K_{\mathrm{II}}^{\mathrm{LR}}}{K_{\mathrm{I}}^{\infty}}\right] \tag{38}$$

where g_{I} and g_{II} are linked to Amestoy-Leblond's functions $\left(F_{i,j}\right)$ through the following relation :

$$\begin{cases} g_{\mathrm{I}}(\alpha,\theta)= & \left(F_{\mathrm{I,I}}^{2}(\alpha)+F_{\mathrm{II,I}}^{2}(\alpha)\right)F_{\mathrm{I,I}}^{2}(\theta) \\ & +\left(F_{\mathrm{I,II}}^{2}(\alpha)+F_{\mathrm{II,II}}^{2}(\alpha)\right)F_{\mathrm{II,I}}^{2}(\theta) \\ & +2\left(F_{\mathrm{I,I}}(\alpha)F_{\mathrm{I,II}}(\alpha)+F_{\mathrm{II,I}}(\alpha)F_{\mathrm{II,II}}(\alpha)\right) \\ & \cdot F_{\mathrm{I,I}}(\theta)F_{\mathrm{II,I}}(\theta) \\ g_{\mathrm{II}}(\alpha,\theta)= & 2\left(F_{\mathrm{I,I}}^{2}(\alpha)+F_{\mathrm{II,I}}^{2}(\alpha)\right)F_{\mathrm{I,I}}(\theta)F_{\mathrm{I,II}}(\theta) \\ & +\left(F_{\mathrm{I,II}}^{2}(\alpha)+F_{\mathrm{II,II}}^{2}(\alpha)\right)F_{\mathrm{II,I}}(\theta)F_{\mathrm{II,II}}(\theta) \\ & +2\left(F_{\mathrm{I,I}}(\alpha)F_{\mathrm{I,II}}(\alpha)+F_{\mathrm{II,I}}(\alpha)F_{\mathrm{II,II}}(\alpha)\right) \\ & \cdot\left(F_{\mathrm{I,I}}(\theta)F_{\mathrm{II,II}}(\theta)+F_{\mathrm{II,I}}(\theta)F_{\mathrm{I,II}}(\theta)\right) \end{cases} \tag{39}$$

Appendix B Maximization of $G - G_{\mathrm{c}}$

Use of the GMERR criterion is mandatory to study crack propagation in heterogeneous brittle materials. Unfortunately such a use apparently requires the determination of the full angular distribution of G and G_{c}, implying a heavy and time-consuming numerical procedure. However, let us introduce the following assumptions :

1. the inclusions are tougher than the matrix, $G_{\mathrm{c}}^{\mathrm{inc}} \geq G_{\mathrm{c}}^{\mathrm{mat}}$, whereas the matrix/inclusion interfaces are weaker, $G_{\mathrm{c}}^{\mathrm{int}} \leq G_{\mathrm{c}}^{\mathrm{mat}}$;
2. for the small values of $K_{\mathrm{II}}/K_{\mathrm{I}}$ considered here, G increases until θ takes the value $\theta_{G-max} = \theta_{\mathrm{ini}} - 2\dfrac{K_{\mathrm{II}}^{M}}{K_{\mathrm{I}}^{M}}$, and decreases beyond this value;
3. we only consider angles θ in the interval $\left[-\frac{\pi}{2},\frac{\pi}{2}\right]$.

Then $G - G_{\mathrm{c}}$ can be maximal either inside the open intervals where G_{c} is constant (i.e. in the matrix or the inclusion), or at endpoints of these intervals (i.e. along the matrix/inclusion interface). Thus it is only necessary to compare the values $(G - G_{\mathrm{c}})(\theta_{\mathrm{tan}})$ and $(G - G_{\mathrm{c}})(\theta_{G-max})$.

Appendix C Influence of the mesh size on the effective toughness

One of the main advantage of the proposed numerical method is that it only requires a 1D discretization of the crack front, making the simulations substantially faster. The mesh size Δz may then influence crack propagation and its dynamics in composite materials. The impact of the mesh size Δz on the effective toughness is plotted in Fig. 36.a

We observe that the results converge to a single value when $\Delta z \geq d/16$, where d is the diameter of the inclusion. Discrepancies for coarser mesh size can be attributed to the inclusion geometry the crack actually perceives when it lands on the inclusion (see Fig. 36.(b-e)).

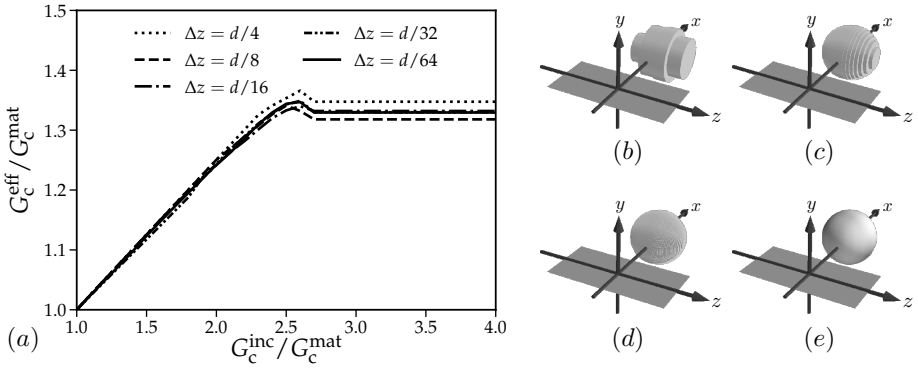

Figure 36: (a) Influence of the front mesh size Δz on the effective toughness G_c^{eff} and on the inclusion geometry actually perceived by the crack in the simulations for (b) $\Delta z = d/4$, (c) $\Delta z = d/16$, (d) $\Delta z = d/64$, and (e) $\Delta z \to 0$.

Appendix D Dynamics of the crossing and by-pass interaction mechanisms

We investigate here the dynamics of both crossing and by-pass mechanisms during the interaction of a crack with periodic arrangements of tough spherical inclusions. The dynamics of the crossing mechanism is illustrated in Fig. 37, where is plotted the in-plane perturbation dynamics in the (zOx) plane are given in Fig. 37.a. The propagation of the central point of the crack front at $z = 0$ in the (xOy) plane along with macroscopic loading G^∞ is given in Fig. 37.b. We observe that when the crack starts to cross the inclusion, it does not "know" that the width of the defect increases in the propagation direction (Ox). The macroscopic loading keeps increasing after the initial penetration in order to allow for the stable propagation of the crack inside the defect.

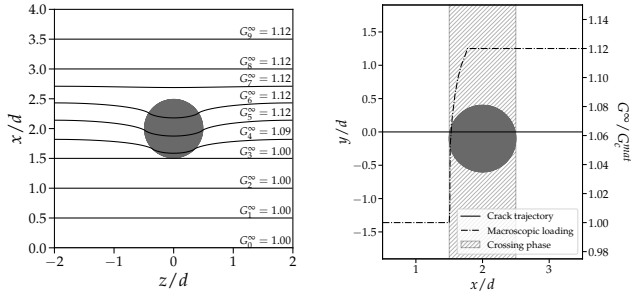

(a) (xOy) plane (b) (zOx) plane

Figure 37: Crossing of periodic arrangements of spherical inclusions with $G_c^{\text{inc}} = 1.5\, G_c^{\text{mat}}$ and $L_z/d = 4$, by a crack landing at $y_{\text{landing}} = 0.1\, d$. In-plane profiles in the (zOx) plane at various loading states (a). Trajectory in the plane (xOy) and macroscopic loading evolution for the center point in $z = 0$ (b).

On the contrary, when the crack chooses to by-pass the inclusion the maximal macroscopic loading is attained at the kinking event (see Fig. 37). During the subsequent by-pass of the inclusion, the crack can realign with the (Ox) direction favored by the macroscopic tensile loading, which facilitates its propagation without requiring any additional increase in the driving force.

During its propagation, the crack select the interaction mode which is energetically more favorable. Yet, as noted by Takei et al. (2013), this choice results from a local maximization of

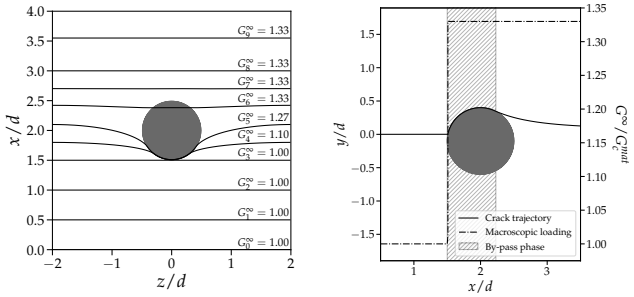

(a) (xOy) plane (b) (zOx) plane

Figure 38: By-pass of periodic arrangements of spherical inclusions with $G_c^{inc} = 3.5\, G_c^{mat}$ and $L_z/d = 4$, by a crack landing at $y_{landing} = 0.1\, d$. In-plane profiles in the (zOx) plane at various loading states (a). Trajectory in the plane (xOy) and macroscopic loading evolution for the center point in $z = 0$ (b).

the dissipation rather than a global one. Such behavior accounts for the fact that the global/partial crossing interaction sometimes prevails over the by-pass one even if such choice is detrimental on a energetic point of view.